ADVANCED OPTICAL MATERIALS
www.advopticalmat.de

Tailored Disorder in Photonics: Learning from Nature

Maximilian Rothammer, Cordt Zollfrank, Kurt Busch,* and Georg von Freymann**

Disorder and photonics have long been seen as natural adversaries and designers of optical systems have often driven systems to perfection by minimizing deviations from the ideal design. Especially in the field of photonic crystals and metamaterials but also for optical circuits, disorder has been avoided as a nuisance for many years. However, starting from the very robust structural colors found in nature, scientists learn to analyze and tailor disorder to achieve functionalities beyond what is possible with perfectly ordered or ideal systems alone. This review article covers theoretical and materials aspects of tailored disorder as well as experimental results. Furthermore selected examples are highlighted in greater detail, for which the intentional use of disorder adds additional functionality or provides novel functionality impossible without disorder.

1. Introduction

Over a period of millions of years, nature has evolved optimized materials and structures for a broad range of functions such as self-cleaning, reversible adhesion, high mechanical strength, thermal insulation, self-healing, and structural coloration.[1–3] Through natural selection, optimally designed nano- and microstructures have arisen for tailored light–matter interactions, even despite a rather limited repertory of materials.[3] Hierarchy is a major reason for the multifunctionality of natural materials such as feathers, which keep the birds body warm and make it water repellant, create wings and tails for aerodynamic lift during flying, and furthermore, provide coloration for camouflage as well as for intraspecific sexual communication.[3–8]

In comparison, mankind just very recently developed fabrication technologies, which can be separated into bottom-up and top-down approaches. In bottom-up approaches, small building blocks (e.g., nanoparticles or molecules) are organized using self-assembly strategies. Bottom-up approaches are scalable and, hence, are suitable for mass fabrication. However, self-assembly always faces the unavoidable risk of introducing unwanted defects (e.g., stacking faults, missing particles), as these processes are not fully controllable. Top-down processes on the other hand allow for full control (within the limits of the precision of the technique). Here, different techniques have been developed for 1D (e.g., atomic-layer deposition, chemical-vapor deposition, molecular beam epitaxy), 2D (e.g., photo-lithography or electron-beam lithography) as well as 3D (e.g., direct laser writing, direct inkjet printing, laser induced forward transfer) structures. With increasing number of dimension, suitability for mass fabrication reduces. However, top-down fabrication reaches the required precision of few tens of nanometers even for 3D approaches to address the length scales present in the intricate structures found in nature.

Due to the growing worldwide interest in photonics, researchers study natural systems as many concepts are resilient against disorder or even utilize certain amounts of disorder to achieve the desired functionality. Coloration derived from the microstructure and the underlying photonic dispersion relations and transport processes play an important role, as these properties can be designed or tailored by controlling the microstructure. Combining the precision of top-down approaches with the flexibility of bottom-up strategies opens new avenues for structures with controlled amounts of disorder. Here, we want to review the mechanisms found in natural structures, briefly discuss the underlying theoretical principles before we provide a broader overview of materials and methods for fabrication. We will conclude with a detailed exposition of four illustrative examples that showcase different aspects of tailored disorder.

M. Rothammer, Prof. C. Zollfrank
Biogenic Polymers
Technische Universität München
94315 Straubing, Germany
E-mail: cordt.zollfrank@tum.de
Prof. K. Busch
AG Theoretische Optik & Photonik
Humboldt-Universität zu Berlin
12489 Berlin, Germany
E-mail: kurt.busch@physik.hu-berlin.de
Prof. K. Busch
Max-Born Institut
12489 Berlin, Germany
Prof. G. von Freymann
Department of Physics and Research Center OPTIMAS
Technische Universität Kaiserslautern
67663 Kaiserslautern, Germany
E-mail: georg.freymann@physik.uni-kl.de
Prof. G. von Freymann
Fraunhofer Institute for Industrial Mathematics ITWM
67663 Kaiserslautern, Germany
The ORCID identification number(s) for the author(s) of this article can be found under https://doi.org/10.1002/adom.202100787.

DOI: 10.1002/adom.202100787

2. Structural Colors and Disorder in Natural Photonics

In nature, structural colors originate from diffraction, interference or scattering of light and many combinations thereof.[9] A couple of the most vivid colors in the animal kingdom are not created by pigments, but by wavelength-selective scattering of light induced by nanostructures.[10] Various animals and plants use them for warning signals, to attract mating partners or sophisticated camouflage to increase the chance for survival of the species.[11,12] These structural colors are based on a highly complex morphology of the epidermis of the organisms. Such natural photonic systems often exhibit a specific disorder which manifests itself by irregularities in the arrangement of the spatial distribution of the architectured materials.[11,13] Thus, stunning displays of coloration, which are highly intense and, in contrast to pigments, do not fade, are generated by the interaction between the visible light and nanoscaled intricate structures that affect polarization, reflection, or absorption.[9,14,15] Some examples of structural coloration in nature are presented in **Figure 1**.

Structural color can be classified into iridescent and non-iridescent.[20] Per definition iridescent colors change in hue or in intensity with the angle of observation or illumination, while non-iridescent colors persist similar in appearance regardless of the viewing angle.[6,21] From a physical point of view, interference as well as diffraction can produce iridescent colors. Besides, certain types of scattering produce non-iridescent structural colors because they originate from irregularities of the structure.[6,22] Most of the structural colors in nature are considered to arise from the following fundamental physical principles and combinations thereof: thin film interference,

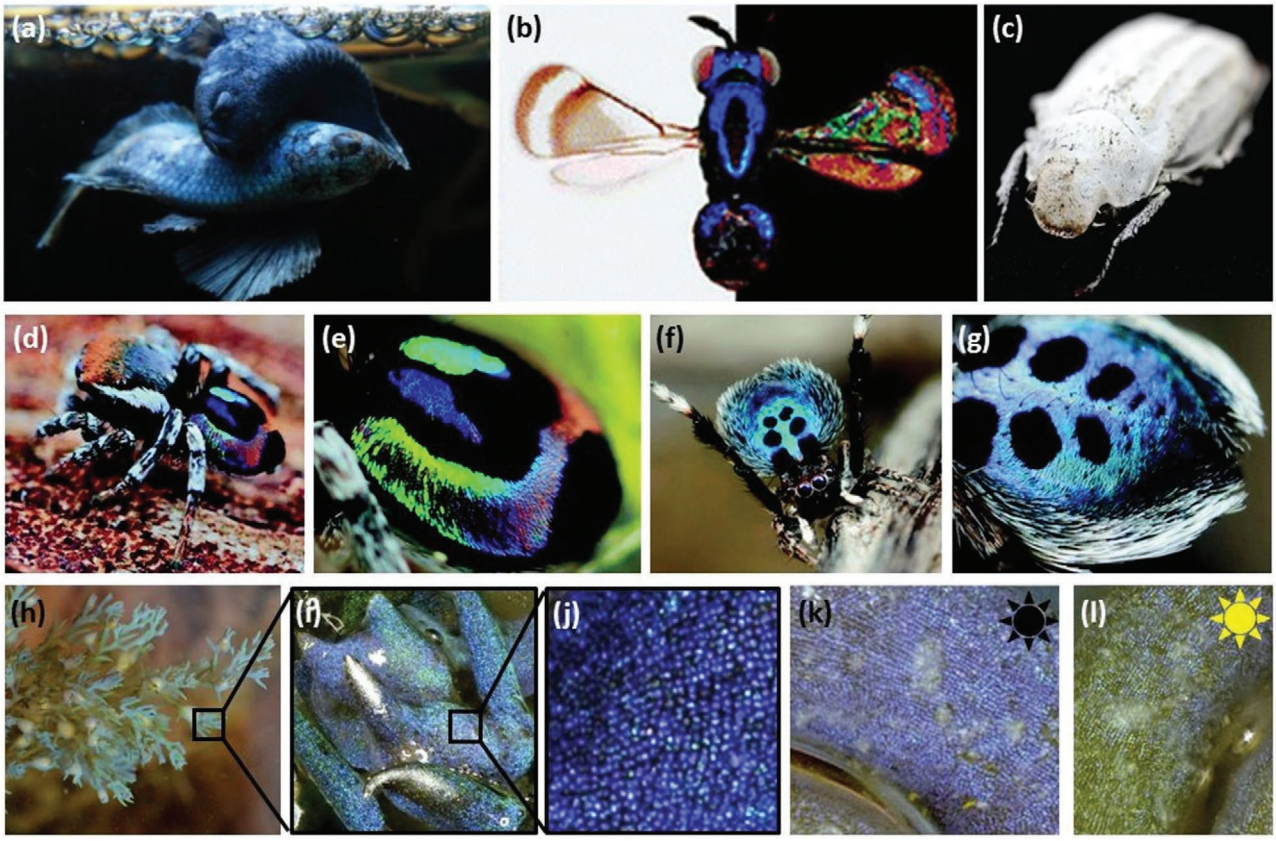

Figure 1. Photographs of flora and fauna revealing structural coloration in nature. a) Siamese fighting fishes (*Betta splendens*) during mating, the blue coloration predominantly occurs through motile iridophores via a multilayer thin film interference phenomenon. This image is courtesy of Jessica Stanzel (Wetzlar, Germany) and adapted with her permission. b) Hymenoptera (*Closterocerus coffeellae*) presenting a characteristic polychromatic color pattern due to thin-film interference against a light absorbing black background, while a light reflecting white background reveals the transparency and the pigmentation of the wing. Adapted with permission.[16] Copyright 2011, National Academy of Sciences. c) The white beetle (*Cyphochilus spp.*) shows an ultra-bright whiteness based on scattering elements that trigger a broadband reflection over the whole range of the visible light. Adapted with permission.[17] Copyright 2013, Nature Publishing Group. d) Diffraction gratings lead to the resulting rainbow iridescence of the male Australian peacock spider (*Maratus robinsoni*). e) Its abdomen displays a strong coloration across the entire visible spectrum of light when it is wiggled. f) Another type of peacock spider (*Maratus nigromaculatus*) generates a more stable coloration arising from a disordered grating architecture. g) Its opisthosoma exhibits a blue angle-independent coloration. d–g) Adapted under the terms of a Creative Commons Attribution CC BY license.[18] Copyright 2020, The Authors, published by The Royal Society of Chemistry. h–j) The brown alga (*Cystoseira tamariscifolia*) reveals a complex 3D opal structure formed from quasi-monodisperse lipid spheres. The alga can tailor the degree of disorder precisely and reversibly in response to the environmental illumination. k) The structural blue coloration is visible at low light ambience. l) In contrast, the blue color vanishes with increasing light intensities. h–l) Adapted under the terms of a Creative Commons Attribution CC BY license.[19] Copyright 2018, The Authors, published by AAAS.

multilayer interference, diffraction grating effects, photonic crystals, and scattering by amorphous photonic materials.[12,23]

Thin film interference is one of the widest spread and simplest structural colorations in nature.[23] A very well-known example of color which is caused by thin film interference is the iridescence of a soap bubble. Another example is the transparent wings of Hymenoptera (*Closterocerus coffeellae*, Figure 1b) that are composed of a membrane of two layers of chitin. This architecture leads to the characteristic polychromatic color patterns that result from variations in the thickness of the wings.[12,16,24–26] Light waves are either reflected or refracted at the boundaries of media with different refractive indices. Light beams reflected at the upper and lower interface interact and create constructive or destructive interference for a distinct angle and wavelength of incident light. An addition of further layers produces a periodic stack which results in an optical material with multiple reflections at the interfaces.[6,12,23]

Multilayer interference produces brighter and more saturated colors than thin film interference.[25] In most biological regimes, structural colors originate in the alternating spatial arrangement of high and low refractive index (n) materials such as chitin ($n \approx 1.56$) and air ($n = 1.0$).[2,24] The appearance of the blue coloration in the Siamese fighting fish (*Betta splendens*, Figure 1a) predominantly occurs through motile iridophores via a multilayered thin-film interference phenomenon of the non-ideal type. Iridophores are color-generating cells, which reflect light by stacks of platelets consisting of guanine ($n = 1.83$), that is one of the highest known refractive indices for a biological material.[2,24,25,27,28]

In nature, there is often a combination of different physical phenomena that produce a structural coloration. The brilliant blue coloration of the Morpho butterfly is based on multilayer interference along the ridges in the vertical direction and diffraction gratings in the horizontal direction, which scatters this color over a large viewing angle.[2,25,29–31] This phenomenon relies on the same physics that is involved in a periodic multilayer stack, except for the orientation of the periodicity of the grating.[6,12,25,26] Without the scattering into different angles, a resulting rainbow iridescence effect can be observed at the Australian peacock spider (*Maratus robinsoni*, Figure 1d,e). The structural color originates from 2D nanogratings on microscale 3D convex surfaces with at least twice the resolving power of a conventional 2D diffraction grating of the same period.[32] During its complex dances to court females, the peacock spider displays every color across the entire visible spectrum of light by raising and wiggling its abdomen.[18,32–34]

Organisms from the flora as well as from the fauna are also able to create structural coloration via photonic crystals, which are periodic dielectric structures in 1D-, 2D-, or 3D-ordered lattices on the order of the wavelength of the visible light.[2,23,25,35] In analogy to electron waves in a solid crystal, the propagation of light in a photonic crystal is described by a photonic band structure.[25,36] Photonic crystals exhibit photonic band gaps that forbid the propagation of light within certain frequency ranges and even exclude the existence of optical modes within specific frequencies depending on the lattice geometry and spacing.[2,12,22,23,37,38] Therefore, a certain wavelength span of the incident light that is corresponding to the forbidden band of the photonic band gap will be selectively reflected, leading to an increase of the color brightness with a rising intensity of the illumination.[39] Biological systems can apply striking 3D photonic crystals in order to generate partial photonic band gaps that provoke brilliant color, which is reflected over a broad angle since 3D periodic crystals manipulate the propagation of light along all directions.[1]

The recently discovered brown alga (*Cystoseira tamariscifolia*, Figure 1h–l) reveals a complex 3D opal structure formed from lipids. The alga is able to control the packing structure of its quasi-monodisperse lipid spheres precisely from an ordered to a disordered level and vice versa. The reflectance of this opaline structure is dynamically responsive to environmental illumination in a manner that the structural color is visible at low light ambience and vanishes completely with increasing light intensities. So far, the biological function of this light-induced reversible color changing mechanism is not fully understood, but there is an indication of a complex interplay between the intracellular 3D photonic structure and photosynthesis.[19]

Scattering of light can also generate structural colors, but it is based on completely different principles than those of multilayer interference or photonic crystals since it originates from structural irregularities.[22,23] Per definition, scattering is the interaction of light, entering a disordered medium with small particles and its consequent deviation from a straight path through random scattering multiple times that provokes a random light emission of the material.[2,12] Light scattering can be classified in phase-dependent scattering that includes interference, reinforcement, thin film reflection and diffraction, and phase-independent scattering which involves Rayleigh, Tyndall, and Mie scattering.[6,25,40] These scattering processes are dominant in amorphous photonic crystals, also known as photonic glasses. They exhibit mainly short-range order between the respective particles while there is no long-range order.[12] Compared to ordered photonic crystals that generate angle-dependent coloration due to the narrow reflection maxima, which is based on the periodicity of the inter-particle distance, photonic glasses produce angle-independent structural coloration.[1,41]

The white beetle (*Cyphochilus spp.*, Figure 1c) has optimized the microstructure of its scales, including the filling fraction, the size, and the distancing of the individual scattering elements as well as a strong scattering anisotropy in order to trigger a broadband reflection over the whole range of the visible light that results in an ultra-bright whiteness and optical brilliance.[12,42–44] A corresponding model structure incorporating all features into very few parameters[45] is discussed in more detail in Section 5.1.

While the above-mentioned iridescence of the spider *Maratus robinsoni* arises from ordered nanogratings, another peacock spider (*Maratus nigromaculatus*, Figure 1f,g) features an approximately angle-independent coloration based on ultradense, curved gratings with a hierarchical disorder.[18] In the course of evolution, various organisms in nature have developed the ability to tailor the degree of disorder in a distinct manner. Photonic crystals are fragmented to create randomly orientated domains, causing a random propagation of light.[1,46] Thus, a local order defines the color while a long-range disorder enables the broadening of the reflectance angle, even in relatively low refractive index materials.[17,35,41]

This interplay between order and disorder can be described as correlation in the arrangement of building blocks forming the structures. In a recent review article, the transition from ordered hyperuniform structures to non-hyperuniform structures with increasing loss of structural correlation is used to describe the amount of disorder in a system.[47] Uncorrelated disorder and the effects on photonic transport properties are nicely covered in recent review articles as well.[48,49]

With respect to precise fabrication, which first of all enables the aspect of tailoring the structural arrangement, we have to differentiate between intrinsic (and mostly uncorrelated) disorder and extrinsic disorder. Intrinsic disorder is present due to fabricational deficiencies like surface roughness or inhomogeneous material distribution or being due to self-assembly processes, which cannot be fully controlled, for example, agglomeration of nanoparticles or stacking faults in self-assembled nanospheres. Intrinsic disorder is stochastic in its nature and can be treated via effective quantities like a diffusion constant. Intrinsic disorder alone is not in the focus of our article, although we will show that it can be used in a very deterministic way to tailor photonic properties. Extrinsic (or tailored) disorder on the other hand is introduced in a deterministic way, so that all deviations from an otherwise ordered structure are known and can be quantitatively described. This includes uncorrelated disorder as well, but in a way, which allows full control on the distribution of the building blocks. This is the field of tailored disorder, where novel properties are introduced and studied in a controlled and reproducible way.

3. Theoretical Background

In this section, we summarize basic notions and effects associated with light propagation in passive random media with uncorrelated disorder, introduce the relevant quantities and approaches for analyzing such systems, and provide a brief perspective on active random media and correlated disorder.

Light propagation in disordered media can be considered on different levels. Disregarding the wave nature of light—loosely speaking, as in a ray-optical description—leads to the consideration of diffusive energy transport, that is, the multiple-scattering of light is treated akin to a random walk and the disordered medium is mapped onto a (spatially dependent) diffusion constant $D(\vec{r})$ for the intensity of light $I(\vec{r},t)$ (see Chapter 9 of ref. [50]). For instance, considerable research and engineering efforts have gone into methods for locating and imaging statistical inhomogeneities such as objects hidden in turbid media[51–54] as well as for quantifying motion on the microscopic scale (e.g., blood flow in tissue and rheological properties of soft matter) via the analysis of the calibrated intensity-autocorrelation function associated with the intensity fluctuations within a speckle spot (see below), the so-called diffusive wave spectroscopy.[55,56] Conversely, it has recently been demonstrated that judicious tailoring of the diffusion constant $D(\vec{r})$ allows the broadband and omni-directional cloaking of objects, so that they do not even cast a shadow.[57] For instance, this can be employed to cloak the contacts in organic light emitting diodes (OLEDS), thereby homogenizing its emission characteristics.[58] We will discuss this approach in more detail in Section 5.3.

Including the wave nature of light modifies the above diffusion picture in several ways. First, if the wavelength is comparable with the size of the scatterer, light can excite the scatterers' geometric resonances, the so-called Mie resonances. For low densities of scatterers, this leads to an additional "dwell time" τ_w per scattering event that has to be added to the time-of-flight τ between two successive scattering events. This results in a strongly frequency-dependent renormalization of the energy transport velocity $v_E = \overline{v}/(1+\tau_w/\tau)$, where $\overline{v}$ represents the transport velocity in the long-wavelength limit[59–61] and translates directly into a corresponding renormalization of the diffusion constant $D = (1/3)v_E l_t = D_0/(1+\tau_w/\tau)$. Here, l_t denotes the transport mean free path and $D_0 = \overline{v}\, l_t/3$ the bare diffusion constant.[50] It should be noted that the transport mean free path l_t which describes the length scales over which the transport direction of energy becomes randomized is distinct from the scattering mean free path l_s which describes the length scale over which the phase of a propagating plane wave is randomized.[50] They are interrelated via $l_t = l_s/(1-g)$, where g is the so-called asymmetry factor. For instance, this asymmetry factor can be tailored by engineering the individual scatterers.[62]

As the scatterer density, n_{scatt}, increases, that is, roughly when, in three spatial dimensions, the distance $d = n_{\text{scatt}}^{1/3}$ between scatterers becomes comparable with the length scale $\sigma^{1/2}$ associated with the scattering cross-section σ, that is, when $\sigma^{1/2} \sim 1/n_{\text{scatt}}^{1/3}$, these strongly wavelength-dependent "dwell time" modifications broaden in frequency and become less pronounced, eventually becoming completely washed out.[63,64]

A second modification of the ordinary diffusion picture is associated with the constructive interference of time-reversed paths in the scattering medium. On the one hand, this leads to the so-called coherent backscattering effect, where an ensemble-averaged enhancement of the backscattered intensity by a factor just below 2 can be observed in a narrow angular range around the direct backscattering direction.[65,66] In fact, a careful theoretical analysis reveals that the width of this backscattering cone is proportional to λ/l_t (λ: wavelength of light) with a proportionality constant close to 1,[67] thus opening a practical way for measuring l_t. On the other hand, enhanced backscattering clearly reduces the diffusion constant. In strongly scattering systems, the corresponding corrections can become as large as the bare diffusion constant itself. In other words, sufficiently strong disorder may bring the diffusion of light to a complete halt, a phenomenon which has first been predicted for non-interacting electron waves[68] and, when adapted to light waves, is known as Anderson localization of light (see ref. [69] for a review on coherent backscattering and Anderson localization of light). Owing to its fundamental importance regarding our understanding of wave propagation, Anderson localization of light has been and still is being investigated from various angles as well as in systems with different types of disorder (see, e.g., refs. [70–72]).

Finally, the interference of (light) waves associated with multiple scattering processes within random media leads to the formation of spatially randomly varying intensity patterns. These so-called speckle patterns may also be observed on a screen outside the random media, and, in principle, such a pattern

contains significantly more information about the associated random medium than what can be obtained within the diffusion approximation. At this point, it is worth to recall that the aforementioned diffusive wave spectroscopy analyzes, in one spatially fixed speckle spot, the temporal intensity correlations that are created by a temporarily varying random medium. Thus, diffusing wave spectroscopy analyzes the "temporal speckle pattern" in one particular spatial location and thereby extracts information about the changes in the random media. As the observation point remains fixed, a treatment of diffusive wave spectroscopy within the diffusion approximation is adequate.

Based on the overall physical picture sketched in the previous section, random media may be modified or tuned in several ways, thus, allowing the tailoring of such systems for numerous application.

For instance, when a gain medium is combined with disorder, the resulting multiple scattering provides a feedback mechanism that can lead to laser-like emission characteristics from the composite system.[73] Specifically, when the multiple scattering is adequately treated within the aforementioned diffusive energy transport framework, this feedback is incoherent and essentially consists in increasing the time a photon spends within the gain region relative to the time of a ballistic flight. If this increased time exceeds the radiative life time of the gain material, a spontaneously emitted photon, on average, triggers more than one stimulated emission before it leaves the gain region. Thus, a "photonic bomb"-like effect,[74,75] akin to amplified spontaneous emission, occurs. Similarly, the "dwell time" renormalization of resonant scatterers may be exploited to tune the emission of such random lasing systems to specific frequencies.[76] A coherent feedback regime of such random lasing systems is realized when the multiple scattering treatment requires the inclusion of coherent-backscattering-type effects.[74,75]

Recently, random lasers for applications in bio-sensing have been realized in self-assembled biocompatible systems[77] and meshes of subwavelength waveguides.[78] Similarly, random-laser-based super-resolution spectroscopy has been demonstrated very recently.[79]

Tuning the correlations of scatterers in disordered systems represents another fascinating handle to tailor the optical properties of random media. For instance, assembling random distributions of mono-disperse spheres with filling fractions near the random packing limit spawns the novel material class of so-called photonic glasses (which could also be called amorphous opals)[80,81] which lend themselves to the tailoring of structural colors.[82] By the same token, random media with hyperuniformly distributed scatterers facilitate the creation of nearly isotropic complete photonic band gaps even for rather low index contrasts between the constituent materials.[83] Recently, a hyperuniformly disordered platform for near-IR waveguiding applications in silicon systems has been realized[84] and the utility of hyperuniform structures for *k*-space based engineering of structural colors has been established.[85,86] Hyperuniform system are treated in more detail in Section 5.2.

Besides the aforementioned tailoring of correlations or gain in random media for, respectively, creating structural-color and random-lasing applications, there exists another class of applications that hinges on tailoring the input to and/or analyzing the output (i.e., the speckle pattern), from random media.

For instance, carefully crafting the structure of the radiation that excites a random medium in terms of frequency spectrum as well as amplitude- and polarization-structure of the relevant spectral range allows to employ the random medium as an effective lensing system for focusing and/or imaging application.[87] Such approaches analyze the correlations of the speckle pattern emerging from an illuminated random sample in space and frequency and from this derive a feedback so that the illumination can be iteratively improved for realizing a desired functionality. Related imaging approaches analyze the speckle patterns that results from fluorescent objects that are hidden in turbid media.[88] The resulting resolution considerably exceeds the resolution that can be obtained within the diffusive energy transport approximation. Similarly, a careful analysis of the speckle pattern from the aforementioned diffusive cloaks actually allows to uncloak cloaked objects.[89] Further, based on the insight that knowing the transmission matrix through a random medium can be utilized for the construction of polarimeters and spectrometers,[90] considerable research efforts have been directed toward the creation of efficient and broadband integrated random spectrometers, first based on 2D silicon photonic-crystal architectures for applications in the telecom bands[91] and recently in standard integrated optical layout based on silicon-nitride waveguiding structures for operation from the visible to the telecom frequency ranges[92,93] (see also **Figure 2**). Specifically, the latter platform has been demonstrated to operate down to the single photon level.[94]

Besides the utility of such integrated single-photon random spectrometers for quantum technologies, disordered photonic structures can also serve as quantum simulators. For instance, in the frequency domain guided light propagation within fibers or 1D waveguides can efficiently be described by the forward Helmholtz equation. As this equation can directly be mapped onto the Schrödinger equation where the propagation distance of the former corresponds to an "effective time," randomizing the propagation constants of the waveguiding element in propagation direction corresponds to the introduction of a time-dependent fluctuating potential in the latter. In other words, coupled waveguiding systems excited by quantum light lend themselves to the quantum simulation of decoherence processes. For instance, recently, a corresponding theoretical framework for analyzing the associated quantum correlations in such systems has been developed[96] and corresponding experiments have confirmed the existence of so-called decoherence-free subspaces for indistinguishable photons.[97] Such coupled-waveguide based systems are discussed in more detail in Section 5.4.

4. Materials, Processes, and Applications for Tailored Disordered Architectures

In the following section, materials, production methods, and promising future applications as well as actual implementations that enable tailored disordered arrangements or benefit from them are described and visualized in **Figure 3**. A well-known method that is used to generate tailored disordered

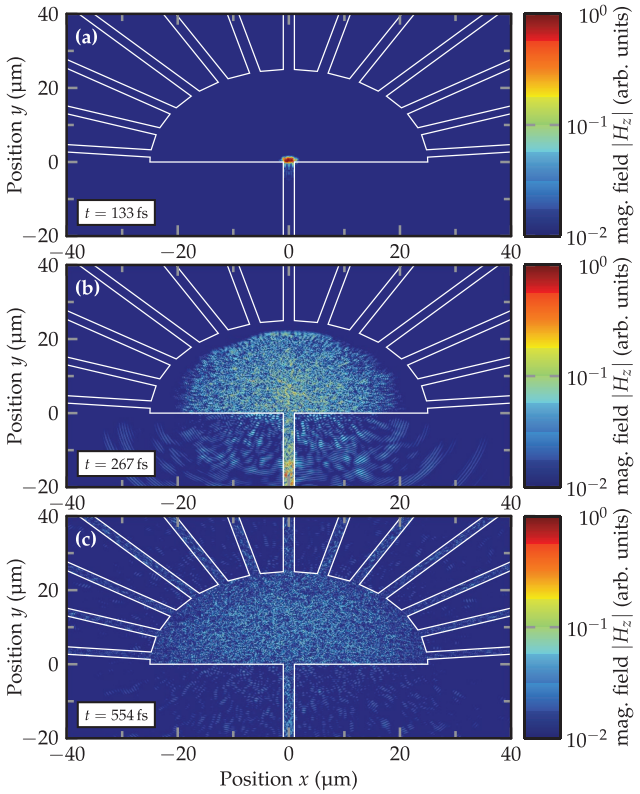

Figure 2. Illustration of the design and operation principle of a silicon-nitride based integrated random spectrometer by a combination of multiple-scattering theory and direct simulations (only the direct simulations are shown). a) A pulse of guide waves enters into a semi-circular area of a planar waveguide that comprises the heart of the random spectrometer. This semi-circular region contains randomly positioned pores and its radius is determined via multiple-scattering theory such that the diffusive regime is realized for the multiply scattered input pulse. This makes the device operation, specifically its spectral resolution, independent of the actual positions of the pores. b) Through multiple scattering events, the major part of the input pulse propagates into the random spectrometer while a smaller part is backscattered into the input waveguide or scattered out of the spectrometer. c) Eventually, the diffusing pulse reaches the edge of the semi-circular region where several output waveguides read out the speckle pattern. A Fourier-transform of these output signals delivers the transmission matrix that fully characterizes the device operation in the frequency range provided by the input pulse. For instance, the decay of the resulting spectral correlation function gives the spectrometer's spectral resolution. For further details we refer to refs. [92,93]. The spectrometer consists of a semi-circular region with radius 25 μm that contains pores with radius 125 nm that cover 9% of the area. The operational wavelength is around 750 nm. The simulations have been carried out with the DGTD finite-element method.[95] Courtesy of Thomas Kiel and Paris Varytis.

structures is the phase separation of strongly immiscible polymers.[98] Here, two polymers, for example, polymethyl methacrylate (PMMA) and polystyrene (PS) are dissolved in an appropriate solvent, mixed, and spin-coated onto a substrate.[99] During the evaporation of the solvent, phase separation of the polymers occurs due to the different polarity of these polymers and leads to a disordered alignment of the respective polymers.[100] These disordered arrays can be tailored in a manner of regulating the mean feature size via adjusting the processing parameters such as tuning the mass ratio of the polymers, their molecular weights, and the applied solvent and the solvent concentration.[98–101] Through this self-assembly process, also nanoscaled disordered patterns are achievable that can be used to fabricate light trapping structures for thin film solar cells.[102] Thin-film photovoltaic cells represent an efficient and sustainable technology for sunlight harvesting, since it exhibits a lower material consumption and hence possibly lower production costs compared to other solar cells. However, these advantages are connected with a significant loss of absorption of the incident irradiation due to the lower amount of employed material. This leads to a lower short-circuit current density.[103,104]

In order to overcome this limitation, for example, bioinspired nanostructures are deployed, which possess efficient incoupling and light trapping capabilities in combination with a high angular robustness. Thus, the absorption of incident light by thin and ultra-thin layers of inorganic (such as amorphous silicon) and organic materials is enhanced.[101,103] The fraction of PS is removed through a selective etching process from the phase separation patterned binary polymer arrangement of PS and PMMA. This induces the formation of nanoholes that are structurally disordered in a tailored manner with respect to their distribution. In a subsequent reactive ion etching step, the nanoholes are transferred into a hydrogenated amorphous silicon layer by employing the patterned PMMA layer as an etching mask (Figure 3e). Thus, a thin photovoltaic absorber of disordered nanoholes is generated, mimicking the architecture of the wings of the black butterfly (*Pachliopta aristolochiae*) that harvests sunlight over a wide spectral and angular range. This bioinspired adaptation enables an improved light harvesting through an enhanced absorption over the entire spectral range, achieving a relative integrated absorption increase of 90% at normal incident angle of light to about 200% at large incident angles.[101]

A further method to improve solar harvesting is the coating of quasi-periodic surface wrinkles as a transmission grating on planar heterojunction crystalline silicon solar cells in order to increase the light absorption. This relies on an efficient incoupling of incoming photons and a recapturing of light that is reflected on the front side of the solar cell.[107] The wrinkling of the all-polymer material is induced via the coating of a thin PMMA film onto a stretched shape-memory polymer substrate which leads to a mechanically directed self-assembled and disordered surface structure during recovering (Figure 3a). The disorder of the wrinkles can be tailored by adjusting their mean periodicity and heights through tuning the fabrication parameters such as the coating thickness (Figure 3b–d) or the applied stretching force.[105,107] These wrinkled structures can be easily replicated into a transparent resist layer that is deposited on the planar front side of a photovoltaic cell.[107]

Another possible application is the utilization of these surface wrinkles to provide flexible OLEDs with broadband light outcoupling properties.[107] Both of these self-assembly processes, the phase separation method as well as the surface wrinkling technique are highly scalable, rapid, and cost-effective.[100,101,107] Therefore, their implementation to different photovoltaic technologies would be economic and ecologically worthwhile.

The mechanism of phase separation can also be applied in additive manufacturing technologies such as direct laser

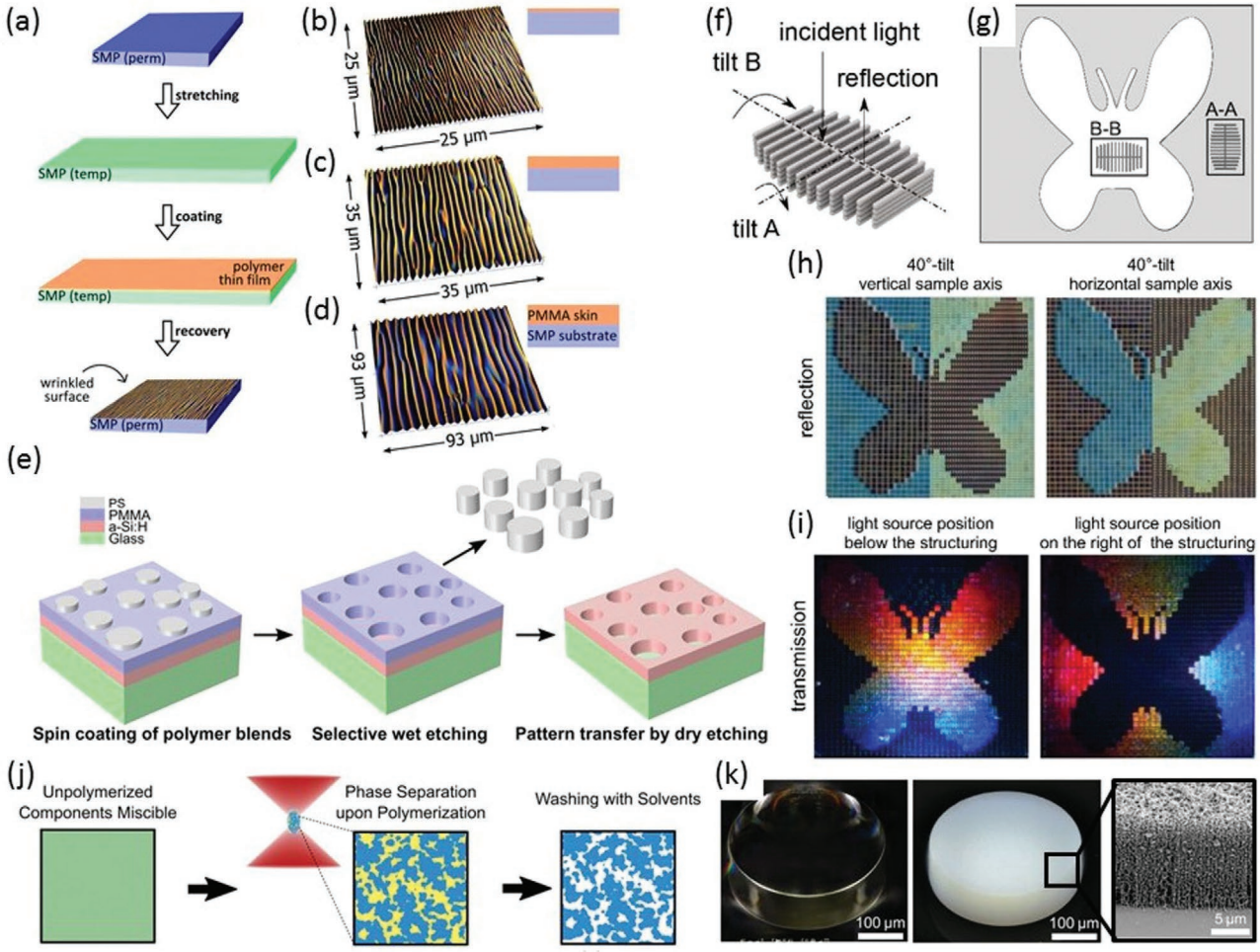

Figure 3. a) Process scheme of fabricating surface wrinkles. A shape-memory polymer (SMP) is stretched from its permanent state (perm) to a temporary form (temp). Then, the elongated substrate is coated with a thin layer of polymethyl methacrylate (PMMA). During recovering of the SMP, the substrate shrinks. This leads to a surface distortion and hence to a wrinkled structure. The size of the wrinkles can be tuned via the thickness of the coated PMMA film from approximately b) 700 nm, c) 1.5 µm to d) 5 µm. a–d) Adapted with permission.[105] Copyright 2017, The Royal Society of Chemistry. e) Schematic of the production of a bioinspired thin photovoltaic absorber of disordered nanoholes. After the evaporation of the solvent, the spin-coated polymers PMMA and polystyrene (PS) separate into two phases. Thus, the fraction of PS is removed through a selective etching process. This leads to a template for the transfer of the nanoholes into the hydrogenated amorphous silicon layer (a-Si:H) via a reactive ion etching step. Adapted with permission.[101] Copyright 2017, The Authors, published by AAAS. f) Photonic coloration originates from an arc structure that can be tilted in two directions. Adapted with permission.[14] Copyright 2019, Optical Society of America. g) Perpendicular arrangement of the arc structures inside and outside of the butterfly geometry that can be employed for anticounterfeiting devices. h,i) The optical properties of the biomimetic architectures in reflection and transmission depend on the tilt direction of the sample or the illumination position. g–i) Adapted under the terms of a Creative Commons Attribution CC BY license.[11] Copyright 2020, The Authors, published by Springer Nature. j) All components of the photoresist are completely miscible in the unpolymerized state, while a polymerization-induced phase separation occurs during the direct laser writing process. A porous polymer structure is achieved by removing the unpolymerized component of the resist. k) The left cylinder is fabricated with a conventional photoresist, whereas the right one is produced with the phase-separating resist. Thus, the left cylinder is solid and appears transparent, while the nanoporous cylinder seems white due to strong light scattering. j,k) Adapted under the terms of a Creative Commons Attribution CC BY license.[106] Copyright 2020, The Authors, published by Wiley-VCH.

writing in order to produce self-assembled nanoporous architectures with mean pore sizes around 50 nm.[106] The especially designed photoresist consists of several components which are completely miscible in the unpolymerized state, while a polymerization-induced phase separation occurs during the direct laser writing process. This leads to the formation of 3D continuous networks of the unpolymerized and the cross-linked species. A porous polymer architecture is obtained by removing the non-polymerized component of the resist (Figure 3j). Thus, the nanopores are filled with air, which provokes light scattering in case the refractive index contrast between the polymer and air is sufficient large enough (Figure 3k). The final porosity of the 3D printed material can be tailored over a wide range via tuning the writing parameters. Generally, the porosity decreases with an increasing laser power. This enables a variety of applications of these nanoporous architectures, for example, in terms of controlling diffuse light scattering, which was already attained by printing miniature Ulbricht light-collection spheres.

Further possible purposes are the application as nanoparticle filters in microfluidics or as scaffolds for cell culture and tissue engineering.[106]

Direct laser writing via two-photon absorption allows also a production of biomimetic nanoarchitectures inspired by the blue Morpho butterfly. This results in a structural coloration with just a small angle dependence through tailoring the degree of disorder within the photonic pattern. This approach enables adjusting of structural colors with a distinct hue such as blue, green, yellow and brown via modifications of the process parameters.[11] For mimicking this complex natural photonic multilayer architecture, the interference-assisted polymerization method is applied,[108] since the resolution of the conventional two-photon polymerization process is too low. This allows an adjustment of the structural features in the range of approximately 20 nm by varying solely the average laser power during the direct laser writing process.[11] Especially, the blue coloration is almost angle-independent, since it reveals several modes of disorder. They are based on the low degree of polymerization due to the operation of the two-photon polymerization at low laser power close to the polymerization threshold.

These inhomogeneities of the multilayer structure in combination with height differences and several tilted areas cause angle-insensitive optical properties in a range of 30° through incoherent scattering for the green and blue hue, while the yellow and brown coloration displays a stronger angle dependence. This originates form the two-photon polymerization at higher average laser power that leads to a higher degree of cross-linking and hence to an absence of disorder.[11] A promising field of applications for such tunable structural coloration can be seen in anticounterfeiting devices (Figure 3f–i) or biomimetic coloration systems.[14] Model structures derived from disorder properties which mimic the optical properties of the Morpho butterfly without reproducing the overall structure[45] are discussed in more detail in Section 5.1.

A new type of bio-based photoresist emerged during the last years that is based on methacrylated polysaccharides such as cellulose,[109] hyaluronic acid,[110,111] dextran,[110] and pullulan[112] and can be applied in two-photon polymerization. This class of resists is derived from renewable resources, hence representing a sustainable and environmentally friendly alternative compared to fossil-based polymers.

Another simple fabrication method to generate 2D nanostructured strongly correlated disordered substrates relies on the self-stabilized colloid deposition. A disordered packing of colloidal spheres exhibits an angle-independent structural coloration in case that the particles are on the scale of the wavelengths of the visible light.[113] This approach is scalable and allows for the tailored fabrication of disordered structures via tuning of the experimental parameters such as the size distribution of colloids or the ionic strength of the dispersion.[85] The nanoparticle patterns are obtained via the attaching of particles onto a substrate due to their opposite charge. Therefore, a support structure that is coated with a thin Al_2O_3 layer is immersed into a colloidal dispersion of PMMA nanospheres. The nanospheres are immobilized at the Al_2O_3 layer due to electrostatic forces. Subsequently, the aqueous solvent is removed via lyophilization in order to avoid an aggregation of the particles. The resulting pattern appears randomly as the nanospheres are not arranged periodically, but it exhibits a common average interparticle distance. This interspace can be tuned by the ionic strength of the dispersion solution such as an increase of the ionic strength leads to a decreasing interparticle distance. This bottom-up process enables a tunable fabrication of optical substrates revealing correlated, in particular, hyperuniform disorder. Hence, it opens up a new class of photonic material for new possibilities of k-space engineering.[85]

5. Examples

In this section, we highlight four selected examples which exemplify the theoretical concepts and experimental approaches summarized in the previous two sections. As the field has been largely inspired by coloration found in nature, we discuss how a model is derived that is capable via variation of only very few parameters to use tailored disorder to achieve coloration as well as brilliant white. This example directly showcases "learning from nature," as it grows beyond mere bio-mimicry by implementing the same functionality as found in nature but in a much more abstract way. In a second example, we show how hyperuniform disorder allows to create photonic bandgaps and functional structures, so far a domain of perfectly ordered structures. In the third example, intrinsic disorder in the form of homogeneously distributed scattering centers is discussed, which is used to create cloaks for diffusive light. As a last example, disorder in coupled waveguide systems is reviewed. In a disordered environment, hopping rates between coupled waveguides can be influenced and propagation in disordered waveguide arrays can be used to control the intensity correlation $g^{(2)}$ from coherent to thermal and even super thermal distribution. Propagation of entangled photons is also briefly discussed.

5.1. Structural Coloration and Brilliant White

As discussed in the overview on how nature utilizes disorder in a very clever way, iridescent as well as non-iridescent coloration and even brilliant whiteness are created from a very limited choice of materials, most of which have a low refractive index ($n < 1.9$) at least compared to semiconductors. In a very early paper on coloration in nature, Vukusic and co-workers argued that only a narrow border should separate the mainly ordered structures like those of the colorful butterflies from the highly scattering white structures found in certain beetles.[42] Materials used and typical dimensions of these structures are very similar; hence, the spatial arrangement has to play a major role.

The non-iridescent blue coloration of the Morpho butterflies as well as the brilliant whiteness of Lepidiota stigma and beetles of genus Cyphochilus are very well studied and the underlying processes understood.[12,18,42–44,114,115]

Here, we want to discuss how to transfer these optimized microstructures to a simple model,[45] which allows reproducing non-iridescent coloration as well as brilliant whiteness with a material of low refractive index ($n = 1.55$) by accounting for the underlying disorder mechanisms. This encompasses the optimized microstructure of the scales, including the filling

fraction, the size, and the distancing of the individual scattering elements as well as their size distribution and spatial arrangement. The goal is to not only reproduce the coloration but also to match the time-resolved and highly anisotropic transport properties of single scales.[43,115]

To achieve coloration, the stop gaps of 1D photonic crystals (Bragg-stacks) are a starting point. Without modification, such a Bragg-stack delivers iridescent colors, which strongly vary with the angle of incidence (or observation). Breaking the Bragg-stack apart into pieces with subwavelength dimensions, for example, a footprint of 300 nm × 300 nm, and shifting these pieces up and down in a random fashion, leads to scattering of the light from the stop gap into all directions and, hence, to non-iridescent angle-independent coloration, thus mimicking the effects found in the scales of the Morpho butterflies. This approach is visualized in **Figure 4**a, where a 2D cross-section of the otherwise 3D structure is depicted. The different Bragg-stacks have all the same period and layer thickness, but they are shifted along the stacking direction. Light impinging from the top is scattered into all directions due to the subwavelength footprint of the individual Bragg-stacks along the in plane directions, leading to non-iridescent coloration, as shown on the right hand side of Figure 4a. Here, finite-difference-time-domain (FDTD) calculations have been used to calculate the angle dependent color distribution. For a certain realization, the blue color is spread into the full half-space above the sample. With several scales with different disorder realizations present, the blue color is even more evenly spread, filling the darker spots observable in the figure.

To achieve brilliant whiteness with the same approach, a close inspection of the materials distribution found in the scales of the white beetles is necessary.[114] One finds that here the coloration stems from a second-order stop gap, which covers due to the disorder all wavelengths in the visible range. Positional disorder as well as thickness variation of the different layers and even missing layers contribute to a structure, which very efficiently scatters light of all visible frequencies into all directions.[45] A schematic sketch of this layout is shown in Figure 4b. Layer thickness and presence of layers are randomly varied with distributions retrieved from the original beetles.[114] This leads to all visible colors scattered into all directions, which create the overall white appearance of the beetle as shown in the FDTD calculations.

These structures can nevertheless be fabricated by 3D direct laser writing and demonstrate the same optical appearance as the beetle scales. A direct comparison between an original beetle scale and the Bragg-stack structure under a light microscope with 10× magnification is depicted in Figure 4c. The light microscopy image in reflection mode clearly shows the different colored speckles expected from the numerical calculations. The structures appear darker than the glass substrate, as light is scattered under larger angles than the numerical aperture of the 10× microscope objective can collect. Observed with the naked eye, scale and model structure appear in the same brilliant white, as shown in Figure 4d. The direct laser written structure is marked with the white arrow and reproduced in the enlarged inset. The scanning electron microscopy top view shown in Figure 4e demonstrates the different Bragg-stacks with their respective footprint (here 1 µm × 1 µm. As the brilliant white is generated from the second order stopband, this model nicely scales. On can easily enlarge the overall periodicity of the Bragg-stack to meet fabricational requirements and still observe the same brilliant whiteness, if one works with the third or even higher order stopbands. This is a direct benefit of this model structure, as it does not require close mimicking of the natural blueprint but utilizes the overall disorder characteristics important for the functionality of the structure.

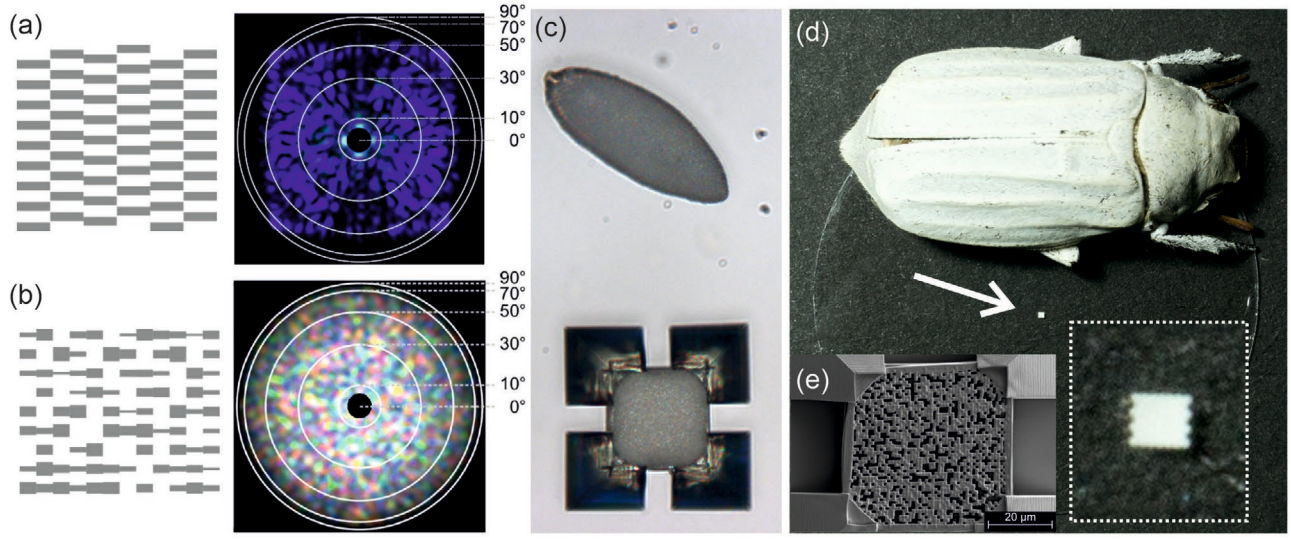

Figure 4. a) Model structure and color distribution for Bragg-stacks. b) Model structure and color distribution for disordered Bragg-stacks. c) Light microscopy image of a single scale and a disordered Bragg-stack structure under medium magnification (10×). The brilliant white dissolves in several colored speckles under this magnification as predicted from the model structure. d) Photograph of a white beetle sitting on a glass substrate with a disordered Bragg-stack structure (see arrow). Clearly, the brilliant white of beetle and structure are visible. The Bragg-stack structure is enlarged in the inset marked with the dotted line. e) SEM image of a fabricated disordered Bragg-stack structure similar to the one shown in (c).

Optical transport measurements and corresponding numerical calculations on the beetle scales and the disordered Bragg-stack structures show similar time-constants and spectral distributions, establishing that the simple model reliably reproduces the optical properties of the intricate beetle scales, although only very few average parameters are required: the average layer distance and distance distribution, the average layer thickness and thickness distribution, and the filling fraction, controlled by the number of layers to be removed.

5.2. Hyperuniformity

As alluded to in Section 3, hyperuniform materials allow for the formation of isotropic but disordered photonic materials, which nevertheless possess complete band gaps for all directions of propagation and for all polarizations.[116] Mathematically, hyperuniform materials can be constructed from an array of points, whose number variance within a spherical sampling window grows slower than the corresponding volume.[116]

Due to the random nature of these network structures, even a large amount of defects, that is, the removal of links in the networks does not lead to a closing of the band gap. In theoretical modelling, up to 58 % of links could be removed without closing the gap completely.[117] Hence, it comes as no surprise that many structures found in nature possessing only a slight amount of incoherent disorder belong to the more general class of hyperuniform materials.

Furthermore, although not as straightforward as in ordered photonic crystals[118] but without the restrictions to the symmetries of photonic crystals, resonators and waveguide structures can be introduced. As a benefit of the homogeneous structure of the hyperuniform materials, waveguide bends can be constructed for almost arbitrary angles.[119] A few examples are depicted in **Figure 5**a–c. For 2D structures, even for a low refractive index contrast of 1.6:1, complete isotropic gaps open, making these structures favorable for experimental realization.

These promising concepts have been extended toward 3D hyperuniform materials, although here higher refractive indices (around $n = 3.6$, even slightly higher than for 3D photonic crystals) are required to open isotropic bandgaps.[122]

Soon after these theoretical proposals, experimental realization of hyperuniform materials have started for microwave radiation. 2D materials consisting of cylinders and connecting walls of commercially available Al_2O_3 building blocks demonstrate complete bandgaps as well as the waveguides with arbitrary bending

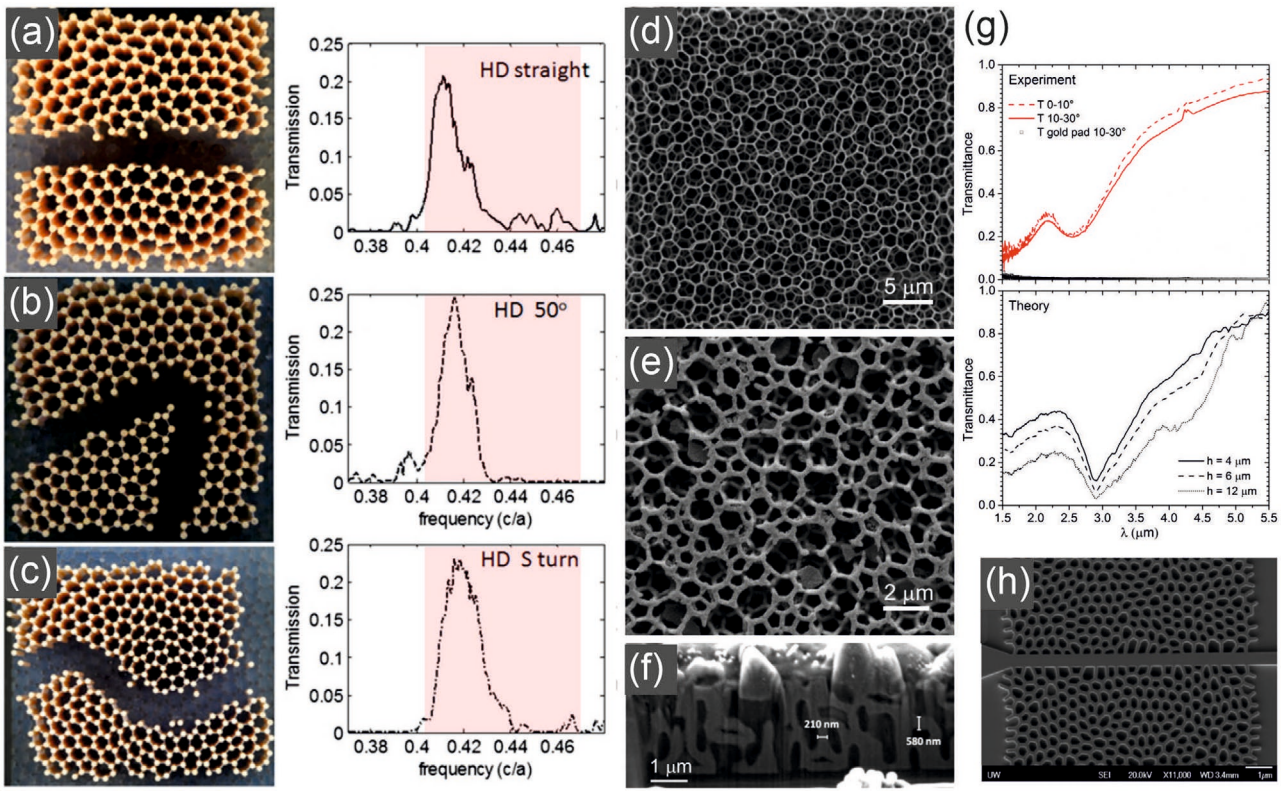

Figure 5. a–c) Different waveguide realizations inside a 2D hyperuniform structure made from Al_2O_3 cylinders and walls designed for operation at microwave frequencies. Transmittance for all three realizations reaches up to 25% inside the bandgap marked in red. HD, hyperuniform defect. Reproduced with permission.[120] Copyright 2013, National Academy of Sciences. d) Realization of a 3D hyperuniform structure made from silicon for operation in the near-infrared. e) Close up of (d). f) Focused ion beam cross-section of the structure showing the materials distribution inside the structure. g) Experimental transmittance spectra of the structure in (d) for two different angle regions (top) compared with theoretical calculations for different sample thickness (bottom). d–g) Reproduced with permission.[121] Copyright 2017, Optical Society of America. h) A 2D hyperuniform structure with an embedded waveguide fabricated in silicon on insulator via e-beam lithography. Reproduced under the terms of a Creative Commons Attribution CC BY license.[84] Copyright 2019, The Authors, published by Springer Nature.

angles[120] (see Figure 5a–c). Cylinders have a radius of $r = 2.5$ mm and the wall a thickness of $t = 0.38$ mm; structures are assembled by hand. At microwave frequencies, the material has a refractive index of $n = 2.96$. Transmittance through these waveguides reaches up to 25% (right hand side of Figure 5a–c). These values are in good agreement with theoretical expectations (not shown).

As hyperuniform materials promise to open bandgaps for smaller refractive index contrast than photonic crystals, that is, for refractive indices of $n < 1.9$, the same group realizes a hyperuniform material via stereolithography from a transparent, polycarbonate-based plastic with refractive index $n = 1.6$[123] (Accura 60 from 3D Systems). Here, an isotropic bandgap for TE polarization in this 2D structure could be experimentally measured at 23.5 GHz. Comparison with photonic crystals as well as quasicrystals fabricated along the same lines demonstrate that hyperuniform materials indeed show the most isotropic and widest bandgap for a given refractive index contrast. 2D realization for microwave frequencies are fabricated via direct printing of Al_2O_3 amorphous gyroid structures, having an isotropic bandgap at around 2.2 GHz.[124]

First 3D realizations of hyperuniform materials targeting bandgaps in the near infrared spectral range use 3D direct laser writing for sample fabrication. Here, the cylinders and walls from the 2D design are replaced by a 3D linked network close to the theoretical suggestion.[117,122] Light scattering measurements in comparison with theoretical expectations confirm the overall hyperuniform arrangement of the material.[125] Further reducing the length of the links from $a = 3.3$ µm to $a = 2$ µm, the same group analyzed in detail the fabrication challenge of hyperuniform materials for telecommunication wavelength around 1.5 µm. They confirm that by scaling down the length of the links, the optical scattering properties scale down too, as expected. Typical experimental deviations as shrinkage or ellipsoidal cross-section of the links do not lead to markable deviations from the theoretical expectations. However, realizing these structures in high-index materials instead of polymer is challenging.

To achieve this, silicon chemical vapor deposition is applied, which has already led to 3D silicon photonic crystals[126] and quasicrystals.[127] The process starts from the polymer template, which is coated with a very thin layer of titania. Subsequently, the polymer is thermally removed, leaving a thin titania hyperuniform network. This network is then coated with the required amount of silicon via chemical vapor deposition.[128] For corresponding structures, see Figure 5d–f. First hints of a gap opening around 3 µm are observed in transmittance spectroscopy, corresponding nicely with theoretical predictions (Figure 5g). However, no angle-dependent measurements are reported to confirm an isotropic gap.[128] Further reduction of the link length down to $a = 1.54$ µm led to a gap positioned around 2.4 µm, which marks so far the shortest wavelength achieved for 3D hyperuniform materials.[121]

2D hyperuniform materials fabricated via electron-beam lithography in a silicon on insulator platform target the bandgap for TE polarization to be centered around 1.55 µm.[84] Waveguides (see Figure 5h) as well as resonators could successfully be integrated. If fabricated in a p+pinn+ configuration (i.e., p-doped silicon, intrinsic silicon, n-doped silicon), electrical tuning becomes possible.

Adding electric aluminum contacts on the p-doped and the n-doped side, a certain tunability of the resonators wavelength sitting in the intrinsic part is achieved. Varying the applied voltage by only 2 V, the resonance can be tuned from 1585.2 to 1583.2 nm. With increasing voltage, the quality factor of the resonator also decreases from above 10^6 down below 10^4. This tunability allows for switching signals with a bandwidth of up to 1 GHz by applying only 70 mV.[84]

5.3. Tailored Diffusion and Cloaking

Optical invisibility cloaking using transformation optics is a successful route to molding the flow of light for ballistic light propagation.[129,130] While here mostly resonant structures are required, broadband, angle-, and polarization-insensitive designs and realizations are scarce and mainly of academic interest. Tailoring the diffusive properties of materials surrounding an object to be concealed allows for very effective cloaking in a stationary sense, rendering the object truly invisible for almost all conceivable way of common real life illuminations.[131] Stationary means, in this context, timescales derived from the time light takes to propagate through the structures. Even diffusive transport of light happens on times much shorter than what even the most sophisticated motion capture cameras are able to detect.[132] Here, intrinsic disorder is used while its spatial distribution is tailored to control the diffusivity of light $D(\vec{r})$.

As discussed in Section 3, when interference effects are neglected, light transport in diffusive media is described via the diffusion equation[131]

$$\vec{\nabla}\cdot\left(D\vec{\nabla}n_{\text{phot}}\right)-\frac{\partial n_{\text{phot}}}{\partial t}=\frac{n_{\text{phot}}}{\tau} \tag{1}$$

n_{phot} is the photon density, τ is the photon lifetime $\tau = l_{\text{abs}}/v_{\text{e}}$, l_{abs} the absorption mean free path length, and v_{e} the energy transport velocity. As the speed of light in media with diffusive transport is still extremely fast, transient phenomena can be neglected so that the stationary version of the diffusion equation is a very good description for the propagation of light:

$$\vec{\nabla}\cdot\left(D\vec{\nabla}n_{\text{phot}}\right)=0 \tag{2}$$

For the diffusivity, we have to use $D = (1/3)v_{\text{e}}l_{\text{t}}$, as described above. As straightforward as this equation looks, care has to be taken, as the model is based on simplifying assumptions,[133] which lead to a few rules-of-thumb:[131] i) $l_{\text{t}} \leq 0.1L$, that is, transport mean free path length is significantly smaller than the smallest extent L of a homogeneously disordered region; ii) $l_{\text{t}} \geq 10\lambda$, that is, transport mean free path length is significantly larger than the wavelength of light; iii) $l_{\text{abs}} \gg l_{\text{s}}$, that is, absorption mean free path length is significantly larger than the scattering mean free path length; iv) photons have travelled a total distance of at least $4 \times l_{\text{t}}$ inside the scattering medium to ensure that every memory of the original direction is lost.

To actually design the diffusivity, the concept of laminates[131] has been proven to be extremely useful, as it also points the way to

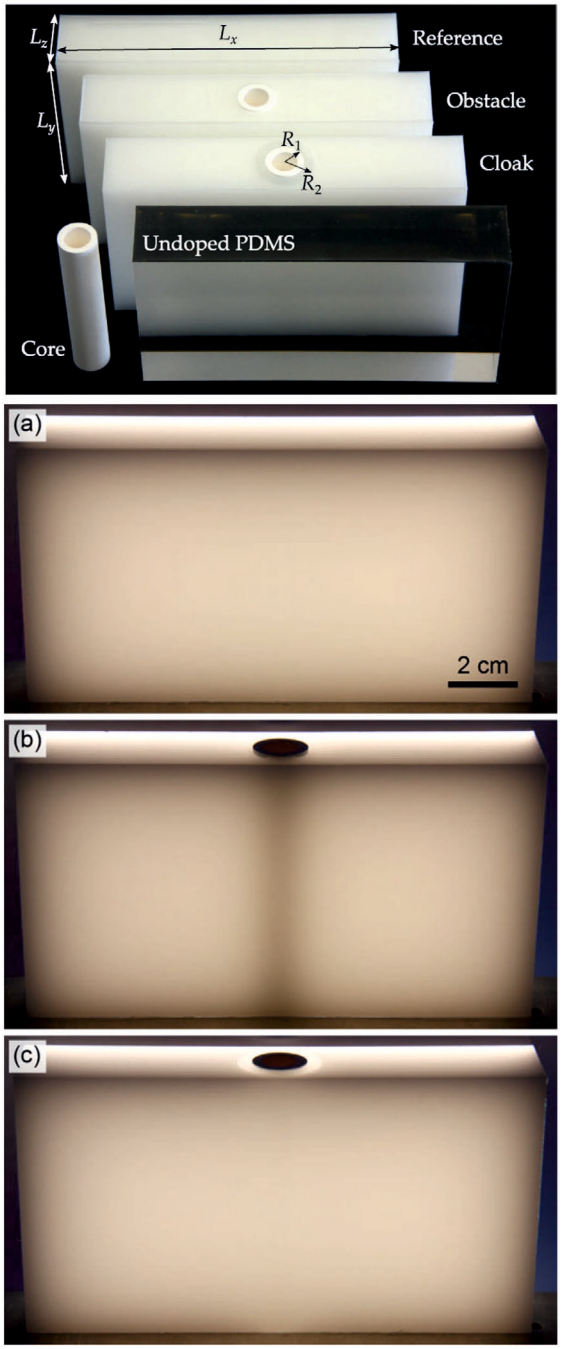

Figure 6. Top panel: Photograph of the reference, obstacle, and cloak sample fabricated of PDMS doped with scattering titania nanoparticles. (An undoped block of PDMS is shown for comparison.) The near-zero-diffusivity cylindrical core (as shown on its own on the left-hand side of the photograph) with radius R_1 embedded in the obstacle sample is surrounded by an additional high-diffusivity shell with radius R_2 in the cloak sample. The faster effective light propagation in this shell makes up for the geometrical detour light has to take around the core. Parameters are: $L_x = 150$ mm, $L_y = 80$ mm, $L_z = 30$ mm, $R_1 = 8$ mm, and $R_2 = 12$ mm. Bottom three panels: Photographs of the three samples when illuminated from behind with a homogeneous white-light source. In panel (b), the near-zero-diffusivity core casts a pronounced diffuse shadow. In contrast, the cloak (c) appears just like the homogeneous reference (a). Reproduced with permission.[134] Copyright 2015, Optical Society of America.

fabrication. To form a laminate, the structure is constructed from at least two materials with different diffusivity, which are stacked in a layered fashion. This allows to guide the light predominantly along the layers with the higher diffusivity, thus allowing to construct even anisotropic diffusivity, that is, leading to a diffusivity tensor and a generalized stationary diffusion equation

$$\vec{\nabla}\cdot(\vec{D}\vec{\nabla}n_{\text{phot}}) = 0 \tag{3}$$

As this equation is form-invariant under coordinate transformations,[131] if the materials are lossless, the same rules known from cloaking for ballistic light transport can be used.[129,130] Light which has to be guided around the object to be cloaked has to travel faster than light passing straight besides the object. Hence, effective cloaking is possible, if the speed of light in the environment is already smaller then the vacuum speed of light. Cloaking objects with a diffusive cloak hence means that the object has to be situated in an already diffusive medium. However, compared to the case of ballistic light transport, the experimentally accessible variability in the speed of diffused light is much higher than for ballistic light transport, allowing for efficient broadband cloaking.

The most simplest design consists of three layers. The innermost layer (the core) has diffusivity $D_0 = 0$, that is, it is a perfectly diffuse reflector, and radius R_1. The second layer (the shell) has diffusivity $D_0 < D_2 < D_1$ and radius R_2. The surrounding medium (the third layer) has diffusivity D_2. The solution for the different diffusivities can be analytically found[134,135] to be

$$\frac{D_1}{D_2} = \frac{R_2^2 + R_1^2}{R_2^2 - R_1^2} \tag{4}$$

This core and shell system has been first realized using a metal cylinder coated with white paint to create the required high diffuse reflectivity surrounded by a layer of PDMS doped with titania nanoparticles to yield high diffusivity. The core–shell structure has been submersed into water, to which white paint had been added such that the diffusivity just matched the analytic expression and the structure appeared to be cloaked.[57] In a modified experiment, water is replaced by another layer of titania doped PDMS, allowing for thinner overall samples and increasing the amount of light transmitted by one order of magnitude (from below 1% to around 7%).[134] This system is depicted in the top part of **Figure 6**. Placing this structure in front of a homogeneous light source, that is, a flat computer screen, the cloaking properties can be observed. Without obstacle, the structure appears completely homogeneous (Figure 6a). Inserting the obstacle, a clear shadow becomes visible, which is almost completely removed by adding the cloak (Figure 6b,c).

As a possible application, these diffusive cloaks can be employed to cloak the wires needed in large area OLED lighting panels.[58,131] For a sketch of the geometry, see **Figure 7**a. Here, for in-room lighting, a diffusive light distribution is desirable; hence, a diffusive cloak will not hinder the overall functionality. At first sight, it comes as a surprise that it is not sufficient to cut the cylindrical cloak in half to achieve proper cloaking of wires on the surface of the light emitter. Instead, a structure with a triangular void around the wire is preferred and allows

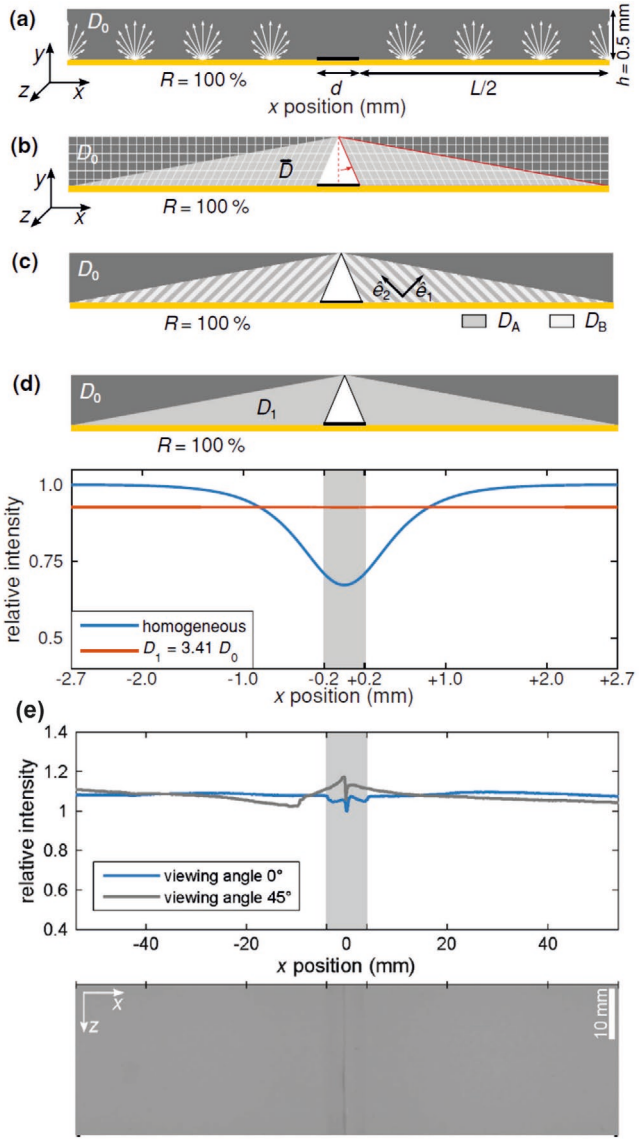

Figure 7. a) Model structure of an OLED: The light emitting area is represented by the yellow line; the opaque contact finger by the black line. a) Homogeneous layer with height h and light diffusivity D_0. b) Ideal coordinate transformation leading to a diffusivity tensor in the light gray regions. The white triangle in the center has a reflectivity of 100%. c) Implementation of (b) by laminate metamaterials composed of alternating layers with isotropic diffusivities $D_{A,B}$. d) Replacement of the laminate structure by a homogeneous and isotropic diffusivity D_1 and resulting intensity calculated using diffusion theory without cloak (blue curve) and with the cloak (red curve). e) Measurements on a realization of the cloak in a scaled up geometry. Line scans under different angles as well as an image demonstrate the overall good functionality. Reproduced with permission.[131] Copyright 2016, Wiley-VCH.

for almost perfect cloaking of the wires, restoring a homogeneous light emission. The required coordinate transformation only affects the x-axis and results in

$$x \to x' = \frac{2hLx + (h-y)(d^2 + dL)}{2h(L+d)} \tag{5}$$

$$y \to y' = y \tag{6}$$

The different variables can be identified in Figure 7a. From this transformation, the diffusivity tensor can be calculated following the recipes in:[58,131]

$$\vec{D} = D_0 \begin{pmatrix} \frac{L}{L+d} + \frac{d^2(L+d)}{4h^2L} & -\frac{d(L+d)}{2hL} \\ -\frac{d(L+d)}{2hL} & \frac{L+d}{L} \end{pmatrix} \tag{7}$$

For the parameter set $d = 0.125L$, $h = 0.1875L$ via diagonalization two diffusivities $D_A \approx 2.50D_0$ and $D_B \approx 0.40D_0$ can be derived, forming an anisotropic laminate structure with the correct anisotropy (see Figure 7c). However, fabrication of such a laminate structure is difficult so that the same reasoning as for the cylindrical cloak can be applied.[131] The lowest possible amount of laminate layers just requires one homogeneous diffusivity $D_1 = 3.41D_0$. Numerical calculation using diffusion theory yields perfect cloaking of the wire (see Figure 7d). In Figure 7e, experimental results are depicted, demonstrating the overall performance of this cloak.

5.4. Coupling and Light Statistics in Disordered Waveguide Systems

As a last example, we want to discuss the field of photonic quantum simulators realized in coupled waveguide systems. Disorder in these systems, allows the observation of novel physical effects not possible in ordered systems and, hence, demonstrates again the importance of tailored disorder. As discussed in Section 3, coupled waveguide systems are of interest for photonic quantum simulation, as the paraxial Helmholtz equation describing the propagation of light in such systems is mathematically equivalent to the time-dependent Schrödinger equation.[136] The propagation direction of light along the waveguides plays the role of the time-evolution of a 2D electronic system and the refractive index difference mimics the potential landscape and the effective mass. Designing the shape of the waveguides allows for introducing artificial gauge fields and hence the realization of effective magnetic and electric fields influencing the photon propagation. Coupled waveguide systems for the simulation of 2D problems require 3D realizations. To date, waveguide systems laser-written in polymeric materials and in glass have been successfully realized. While polymeric systems are more compact due to the higher refractive index contrast ($\Delta n \approx 0.008$–0.01), the influence of intrinsic disorder cannot fully be neglected.[137] The lower refractive index contrast in glass ($\Delta n \approx 9 \times 10^{-4}$)[138] leads to less confinement and larger diameters of the waveguides, the corresponding larger distance to lower coupling constants and overall larger length for a similar amount of hoppings. Here, the same amount of intrinsic fabricational disorder does not play a crucial role any longer. Hence, in the following, we will focus on systems written in glass.

First, the influence of the environment is discussed: Two waveguides with a fixed spacing act as a tuned coupler, transferring energy from one waveguide to the other and back over

the characteristic coupling length. This coupling length can be influenced by the environment, if it is not of constant refractive index but consists of an random amorphous arrangement of waveguides with higher refractive index contrast than the coupled waveguides. It is demonstrated that the effective coupling length decreases in the presence of the amorphous environment.[138] This behavior can be explained in a slight detuning of the respective propagation constants of the two waveguides, due to the disordered environment.

Second, different types of disorder in coupled waveguide systems are analyzed. After the introduction of so-called photonic graphene, that is, waveguides arranged in a honeycomb lattice, and the demonstration of the existence of topologically protected edge states,[139] the stability of these states under uncorrelated composite and structural disorder has been investigated. Composite disorder is realized by varying the refractive index of each waveguide while its spatial position is fixed. For structural disorder, the refractive index of all waveguides is fixed, while the spatial position varies.

The honeycomb lattice can be modeled with the tight-binding equations[140]

$$i\partial_z \psi_n = -\beta_n \psi_n - \sum_m c_{nm}\psi_m \equiv H\psi_n \tag{8}$$

ψ_n is the amplitude of the guided mode in the nth waveguide; the summation is restricted to the nearest neighbors only; c_{nm} is the coupling between the respective waveguides; β_n the propagation constant; and z the propagation direction. The diagonal elements of the resulting Hamiltonian are the propagation constants; the off-diagonal elements are the coupling constants. As refractive index variations change the propagation constants, composite disorder is often called diagonal disorder, while structural disorder is off-diagonal.

As structural disorder preserves the underlying chiral symmetry, the edge states are robust against this type of disorder, while composite disorder leads to a loss on confinement and spreading of the modes into the bulk.[140] Here, chiral symmetry means that eigenmodes form skew-symmetric pairs whose eigenvalues are equal in magnitude but opposite in sign.

In a 1D network with structural disorder (off-diagonal disorder), a light-statistics interferometer has been realized, allowing to tune the light statistics between $g^{(2)} = 1$ (coherent light) over $g^{(2)} = 2$ (thermal light) toward $g^{(2)} = 3$ (super-thermal light) by tailoring the level of disorder $\Delta C = w/\overline{c}$. w is the half-width of a uniform probability distribution of the random coupling coefficients and $\overline{c}$ their mean value. A conventional interferometer is depicted in **Figure 8**a. Light coupled into the two waveguides on the left hand side propagates to the detector

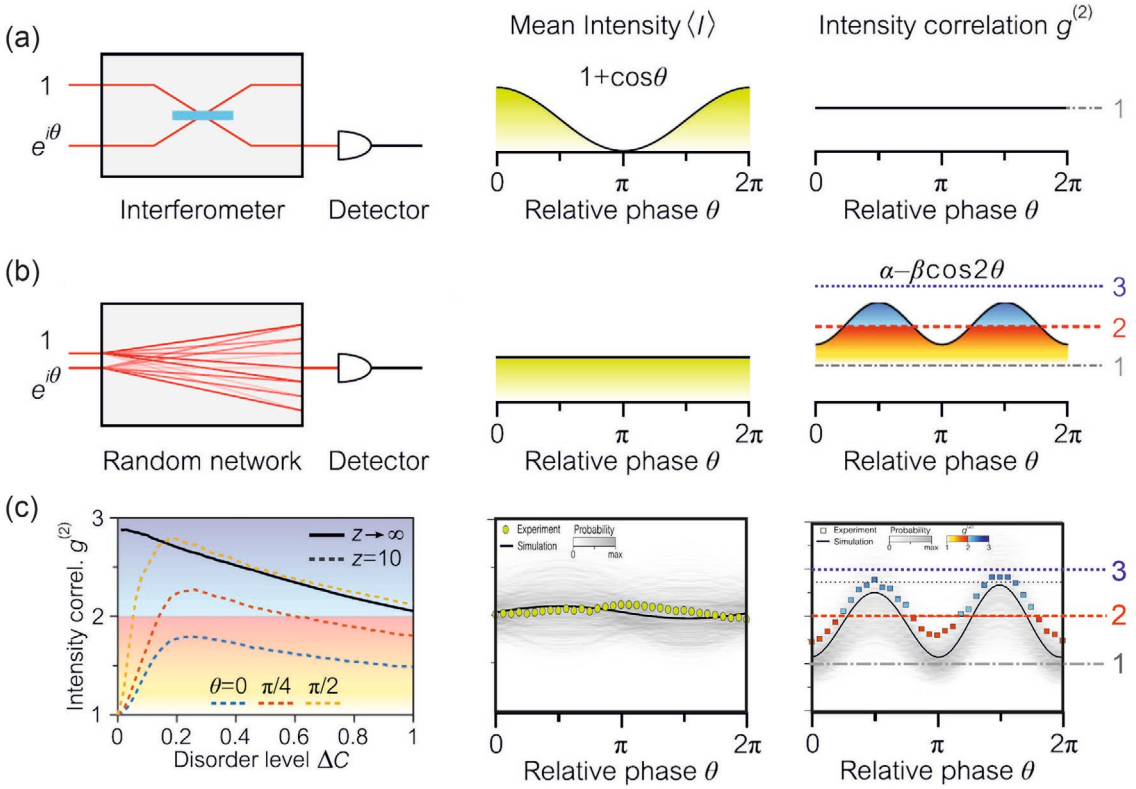

Figure 8. a) Left: Sketch of a typical waveguide interferometer for which one input can be delayed in phase with respect to the other. Center: Phase dependent intensity at the detector. Right: Intensity correlation function $g^{(2)}$ over the two waveguides. b) Left: Random network with two input ports as in (a). Center: Mean intensity at the detector. Right: The intensity correlation function now reaches the thermal or super-thermal region by variation of the phase between the two input fields. c) Left: Intensity correlation function in dependence of the structural disorder in the network and the phase between the inputs. Center: Mean intensity at the detector averaged over several realizations. The almost flat intensity distribution is clearly visible. Right: Input-phase dependent intensity correlation measured for several realizations showing the expected tunability. Adapted with permission.[141] Copyright 2016, Optical Society of America.

on the right. Depending on the phase difference φ between the two path, the output intensity follows the well known cosine shape (Figure 8a, center). The intensity correlation function $g^{(2)}$ between the two outputs stays nevertheless constant.

In contrast, to realize such an light-statistics interferometer, light is coupled into two different waveguides of a 1D network of identical waveguides with structure disorder. A possible realization is depicted in Figure 8b. The light in the two waveguides has to have equal amplitude and a variable but fixed relative phase. Here, the mean intensity at the detector (averaged over several different realizations) stays constant. However, tuning the relative phase allows to change the resulting light statistics $g^{(2)}$ from sub-thermal to super-thermal[141] as schematically depicted on the right hand side.

The above-discussed effects exclusively work for classical light or, equivalently, single-photon quantum light. As a result, the feasibility of engineering complex Hamiltonians using integrated photonic lattices, combined with the availability of entangled photons, raises the intriguing possibility of employing topologically protected entangled states in optical quantum computing and information processing. Achieving this goal, however, is highly nontrivial as topological protection does not straightforwardly extend to multi-particle (back-) scattering. At first, this fact appears to be counterintuitive because, individually, each particle is protected by topology while, jointly, entangled (correlated) particles become highly susceptible to perturbations of the ideal lattice. The underlying physical principle behind this apparent "discrepancy" is that, quantum-mechanically, identical particles are described by states that satisfy an exchange symmetry principle. In a recent work, the physical mechanisms which induce a vulnerability of entangled states in topological photonic lattices have been identified and guidelines for maximizing entanglement without sacrificing topological protection have been obtained.[142]

6. Conclusions

The field of tailored disorder evolved over the last decades. Starting from mere observation and first attempts to learn about the rich optical properties found in nature, first experimental realizations successfully mimicked the natural blueprints. Soon, the theoretical foundation for proper treatment of photonic systems with disorder has been developed, providing researcher with a tool box to apply disorder as a means to design the optical properties.

Based on substantial advancements of nanoscience and -technology through an interdisciplinary research approach of physics, chemistry, biology, computational simulation, and materials science, the methods and materials are continuously improved to enable the generation of new knowledge about tailored disordered photonic nanoarchitectures. These efforts aim to create highly advanced and tunable optical devices.

Tailored disorder is not limited to classical light. Concepts are already employed in photonic quantum simulation[96,97] and first works on the influence of disorder on the transport properties of entangled photons just recently appeared.[142] Understanding the implications of and tailoring disorder will provide quantum-optical systems which are amenable to mass fabrication as they will become as resilient against small fabrication imperfections as classical natural systems already are.

Acknowledgements

This work was funded by the Deutsche Forschungsgemeinschaft (DFG, German Research Foundation) under the priority program DFG-SPP 1839 (ZO 113 21-1, ZO 113 21-2, ZO 113 24-1, ZO 113 24-2, BU 1107/10-1, BU 1107/10-2, BU 1107/12-2, FR 1671/12-1, and FR 1671/12-2). The authors thank Jessica Stanzel for providing a magnificent photo of the Siamese fighting fish, and Dominic T. Meiers and Marie-Christin Heep for the photographs of the white beetle.

Open access funding enabled and organized by Projekt DEAL.

Conflict of Interest

The authors declare no conflict of interest.

Keywords

bio-mimetic materials, coupled waveguides, diffusive cloaking, hyperuniformity, structural color, tailored disorder

Received: April 18, 2021
Revised: May 14, 2021
Published online: June 25, 2021

[1] P. Vukusic, J. R. Sambles, *Nature* **2003**, *424*, 852.
[2] S. Tadepalli, J. Slocik, M. Gupta, R. Naik, S. Singamaneni, *Chem. Rev.* **2017**, *117*, 12705.
[3] B. Bhushan, *Philos. Trans. R. Soc., A* **2009**, *367*, 1445.
[4] T. D. Schultz, O. M. Fincke, *Funct. Ecol.* **2009**, *23*, 724.
[5] P. Vukusic, *Science* **2009**, *325*, 398.
[6] S. M. Doucet, M. G. Meadows, *J. R. Soc. Interface* **2009**, *6*, S115.
[7] M. D. Shawkey, L. D'Alba, *Philos. Trans. R. Soc., B* **2017**, *372*, 20160536.
[8] S. N. Gorb, E. V. Gorb, *Functional Surfaces in Biology III: Diversity of the Physical Phenomena*, Springer, New York **2017**.
[9] B. Song, S. Eom, J. Shin, *Opt. Express* **2014**, *22*, 19386.
[10] E. R. Dufresne, H. Noh, V. Saranathan, S. G. Mochrie, H. Cao, R. O. Prum, *Soft Matter* **2009**, *5*, 1792.
[11] G. Zyla, A. Kovalev, E. L. Gurevich, C. Esen, Y. Liu, Y. Lu, S. Gorb, A. Ostendorf, *Appl. Phys. A* **2020**, *126*, 740.
[12] E. S. Goerlitzer, R. N. Klupp Taylor, N. Vogel, *Adv. Mater.* **2018**, *30*, 1706654.
[13] V. E. Johansen, O. D. Onelli, L. M. Steiner, S. Vignolini, in *Functional Surfaces in Biology III*, Springer, New York **2017**, pp. 53–89.
[14] G. Zyla, A. Kovalev, S. Heisterkamp, C. Esen, E. L. Gurevich, S. Gorb, A. Ostendorf, *Opt. Mater. Express* **2019**, *9*, 2630.
[15] V. Sharma, M. Crne, J. O. Park, M. Srinivasarao, *Science* **2009**, *325*, 449.
[16] E. Shevtsova, C. Hansson, D. H. Janzen, J. Kjærandsen, *Proc. Natl. Acad. Sci. USA* **2011**, *108*, 668.
[17] D. S. Wiersma, *Nat. Photonics* **2013**, *7*, 188.

[18] B. D. Wilts, J. Otto, D. G. Stavenga, *Nanoscale Adv.* **2020**, *2*, 1122.
[19] M. Lopez-Garcia, N. Masters, H. E. O'Brien, J. Lennon, G. Atkinson, M. J. Cryan, R. Oulton, H. M. Whitney, *Sci. Adv.* **2018**, *4*, eaan8917.
[20] M. D. Shawkey, N. I. Morehouse, P. Vukusic, *J. R. Soc. Interface* **2009**, *6*, S221.
[21] D. Osorio, A. D. Ham, *J. Exp. Biol.* **2002**, *205*, 2017.
[22] S. Kinoshita, S. Yoshioka, J. Miyazaki, *Rep. Prog. Phys.* **2008**, *71*, 076401.
[23] S. Kinoshita, S. Yoshioka, *ChemPhysChem* **2005**, *6*, 1442.
[24] A. R. Parker, *J. Opt. A: Pure Appl. Opt.* **2000**, *2*, R15.
[25] J. Sun, B. Bhushan, J. Tong, *RSC Adv.* **2013**, *3*, 14862.
[26] B. Bhushan, in *Structural Coloration*, Springer International Publishing, Cham **2018**, pp. 879–910.
[27] G. Zhang, A. Hirsch, G. Shmul, L. Avram, N. Elad, V. Brumfeld, I. Pinkas, Y. Feldman, R. Ben Asher, B. A. Palmer, L. Kronik, L. Leiserowitz, S. Weiner, L. Addadi, *J. Am. Chem. Soc.* **2019**, *141*, 19736.
[28] M. Amiri, H. M. Shaheen, *Micron* **2012**, *43*, 159.
[29] S. Kinoshita, S. Yoshioka, K. Kawagoe, *Proc. R. Soc. London, B* **2002**, *269*, 1417.
[30] S. Berthier, E. Charron, J. Boulenguez, *Insect Sci.* **2006**, *13*, 145.
[31] P. Ball, *Sci. Am.* **2012**, *306*, 74.
[32] B.-K. Hsiung, R. H. Siddique, D. G. Stavenga, J. C. Otto, M. C. Allen, Y. Liu, Y.-F. Lu, D. D. Deheyn, M. D. Shawkey, T. A. Blackledge, *Nature Commun.* **2017**, *8*, 2278.
[33] D. G. Stavenga, J. C. Otto, B. D. Wilts, *J. R. Soc., Interface* **2016**, *13*, 20160437.
[34] D. E. McCoy, V. E. McCoy, N. K. Mandsberg, A. V. Shneidman, J. Aizenberg, R. O. Prum, D. Haig, *Proc. R. Soc., B* **2019**, *286*, 20190589.
[35] C. Zollfrank, *Scr. Mater.* **2014**, *74*, 3.
[36] Y. Y. Diao, X. Y. Liu, G. W. Toh, L. Shi, J. Zi, *Adv. Funct. Mater.* **2013**, *23*, 5373.
[37] J. Ge, Y. Yin, *Angew. Chem., Int. Ed.* **2011**, *50*, 1492.
[38] K. Kertész, G. Piszter, E. Jakab, Z. Bálint, Z. Vértesy, L. P. Biró, *Appl. Surf. Sci.* **2013**, *281*, 49.
[39] L. Biró, *Mater. Sci. Eng., B* **2010**, *169*, 3.
[40] R. O. Prum, R. H. Torres, *Integr. Comp. Biol.* **2003**, *43*, 591.
[41] L. Schertel, L. Siedentop, J.-M. Meijer, P. Keim, C. M. Aegerter, G. J. Aubry, G. Maret, *Adv. Opt. Mater.* **2019**, *7*, 1900442.
[42] P. Vukusic, B. Hallam, J. Noyes, *Science* **2007**, *315*, 348.
[43] M. Burresi, L. Cortese, L. Pattelli, M. Kolle, P. Vukusic, D. Wiersma, U. Steiner, S. Vignolini, *Sci. Rep.* **2014**, *4*, 6075.
[44] F. Zeighami, M. A. Tehran, *J. Ind. Text.* **2016**, *46*, 495.
[45] D. Meiers, M.-C. Heep, G. von Freymann, *APL Photon.* **2018**, *3*, 100802.
[46] J.-F. Colomer, P. Simonis, A. Bay, P. Cloetens, H. Suhonen, M. Rassart, C. Vandenbem, J. P. Vigneron, *Phys. Rev. E* **2012**, *85*, 011907.
[47] S. Yu, C.-W. Qiu, Y. Chong, S. Torquato, N. Pakr, *Nat. Rev. Mater.* **2021**, *6*, 226.
[48] D. Wiersma, *Nat. Photonics* **2013**, *7*, 188.
[49] C. López, *Adv. Opt. Mater.* **2018**, *6*, 1800439.
[50] A. Ishimaru, *Wave Propagation and Scattering in Random Media*, vol. 2, Academic Press, New York **1978**.
[51] P. N. den Outer, T. M. Nieuwenhuizen, A. Lagendijk, *J. Opt. Soc. Am. A* **1993**, *10*, 1209.
[52] S. Colak, D. Papaioannou, G.'t Hooft, M. van der Mark, H. Schomberg, J. Paaschens, J. Melissen, N. van Asten, *Appl. Opt.* **1997**, *36*, 180.
[53] K. Furutsu, *J. Opt. Soc. Am. A* **1998**, *15*, 1371.
[54] J. Paaschens, G.'t Hooft, *J. Opt. Soc. Am. A* **1998**, *15*, 1797.
[55] G. Maret, P.-E. Wolf, *Z. Phys. B* **1987**, *65*, 407.
[56] D. J. Pine, D. A. Weitz, P. M. Chaikin, E. Herbolzheimer, *Phys. Rev. Lett.* **1988**, *60*, 1134.
[57] R. Schittny, M. Kadic, T. Bückmann, M. Wegener, *Science* **2014**, *345*, 427.
[58] F. Mayer, R. Schittny, A. Egel, A. Niemeyer, J. Preinfalk, U. Lemmer, M. Wegener, *Adv. Opt. Mater.* **2016**, *4*, 740.
[59] M. P. van Albada, B. A. van Tiggelen, A. Lagendijk, A. Tip, *Phys. Rev. Lett.* **1991**, *66*, 3132.
[60] B. A. van Tiggelen, A. Lagendijk, M. P. van Albada, A. Tip, *Phys. Rev. B* **1992**, *45*, 12233.
[61] R. Sapienza, P. García, J. Bertolotti, M. Martín, A. Blanco, L. Vina, C. López, D. Wiersma, *Phys. Rev. Lett.* **2007**, *99*, 233902.
[62] P. Varytis, K. Busch, *Opt. Express* **2020**, *28*, 1714.
[63] K. Busch, C. M. Soukoulis, *Phys. Rev. Lett.* **1995**, *75*, 3442.
[64] J. Gomez Rivas, R. Sprik, C. M. Soukoulis, K. Busch, A. Lagendijk, *Europhys. Lett.* **1999**, *48*, 22.
[65] M. P. van Albada, A. Lagendijk, *Phys. Rev. Lett.* **1985**, *55*, 2692.
[66] P.-E. Wolf, G. Maret, *Phys. Rev. Lett.* **1985**, *55*, 2696.
[67] E. Akkermans, P.-E. Wolf, R. Maynard, *Phys. Rev. Lett.* **1986**, *56*, 1471.
[68] P. W. Anderson, *Phys. Rev. Lett.* **1957**, *109*, 1492.
[69] C. M. Aegerter, G. Maret, *Prog. Opt.* **2009**, *52*, 1.
[70] T. Sperling, W. Bührer, C. M. Aegerter, G. Maret, *Nat. Photonics* **2013**, *7*, 48.
[71] G. Conley, M. Burresi, F. Pratesi, K. Vynck, D. Wiersma, *Phys. Rev. Lett.* **2014**, *112*, 143901.
[72] L. S. Froufe-Peréz, M. Engel, J. J. Sáenz, F. Scheffold, *Proc. Natl. Acad. Sci. USA* **2017**, *114*, 9570.
[73] N. Lawandy, R. Balachandran, A. Gomes, E. Sauvain, *Nature* **1994**, *368*, 436.
[74] H. Cao, *Waves Random Media* **2003**, *13*, R1.
[75] D. S. Wiersma, *Nat. Phys.* **2008**, *4*, 359.
[76] S. Gottardo, R. Sapienza, P. D. Garcia, A. Blanco, D. S. Wiersma, C. López, *Nat. Photonics* **2008**, *2*, 429.
[77] S. Caixeiro, M. Gaio, B. Marelli, F. G. Omenetto, R. Sapienza, *Adv. Opt. Mater.* **2016**, *4*, 998.
[78] M. Gaio, D. Saxena, J. Bertolotti, D. Pisignano, A. Camposeo, R. Sapienza, *Nat. Commun.* **2019**, *10*, 226.
[79] A. Boschetti, A. Tschin, P. Bartolini, A. K. Tiwari, L. Pattelli, R. Torre, D. S. Wiersma, *Nat. Photonics* **2020**, *14*, 177.
[80] P. D. Garcia, R. Sapienza, A. Blanco, C. López, *Adv. Mater.* **2007**, *19*, 2597.
[81] P. Garcia, R. Sapienza, C. López, *Adv. Mater.* **2010**, *22*, 12.
[82] G. Shang, L. Maiwald, H. Renner, D. Jalas, M. Dosta, S. Heinrich, A. Petrov, M. Eich, *Sci. Rep.* **2018**, *8*, 7804.
[83] M. Florescu, S. Torquato, P. J. Steinhardt, *Proc. Natl. Acad. Sci. USA* **2009**, *106*, 20658.
[84] M. Milosevic, W. Man, G. Nahal, P. Steinhardt, S. Torquato, P. Chaikin, T. Amoah, B. Yu, R. Mullen, M. Florescu, *Sci. Rep.* **2019**, *9*, 20338.
[85] P. M. Piechulla, L. Muehlenbein, R. B. Wehrspohn, S. Nanz, A. Abass, C. Rockstuhl, A. Sprafke, *Adv. Opt. Mater.* **2018**, *6*, 1701272.
[86] L. Maiwald, S. Lang, D. Jalas, H. Renner, A. Petrov, M. Eich, *Opt. Express* **2018**, *26*, 11352.
[87] A. P. Mosk, A. Lagendijk, G. Lerosey, M. Fink, *Nat. Photonics* **2012**, *6*, 283.
[88] J. Bertolotti, E. G. van Putten, C. Blum, A. Lagendijk, W. Vos, A. P. Mosk, *Nature* **2012**, *491*, 232.
[89] A. Niemeyer, F. Mayer, A. Naber, M. Koirala, A. Yamilov, M. Wegener, *Opt. Lett.* **2017**, *42*, 1998.
[90] T. W. Kohlgraf-Owens, A. Dogariu, *Opt. Lett.* **2010**, *35*, 2236.
[91] B. Redding, S. F. Liew, R. Sarma, H. Cao, *Nat. Photonics* **2013**, *7*, 746.

[92] P. Varytis, D.-N. Huynh, W. Hartmann, W. Pernice, K. Busch, *Opt. Lett.* **2018**, *43*, 3180.
[93] W. Hartmann, P. Varytis, H. Gehring, N. Walter, F. Beutel, K. Busch, W. Pernice, *Adv. Optical Mater.* **2020**, *8*, 1901602.
[94] W. Hartmann, P. Varytis, H. Gehring, N. Walter, F. Beutel, K. Busch, W. Pernice, *Nano Lett.* **2020**, *20*, 2625.
[95] K. Busch, M. König, J. Niegemann, *Laser Photon. Rev.* **2011**, *5*, 773.
[96] A. Perez-Leija, R. de Jesus Leon-Montiel, J. Sperling, H. Moya-Cessa, A. Szameit, K. Busch, *J. Phys. B* **2018**, *51*, 024002.
[97] A. Perez-Leija, D. Guzman-Silva, R. de Jesus Leon-Montiel, M. Gräfe, M. Heinrich, H. Moya-Cessa, K. Busch, A. Szameit, *npj Quantum Information* **2018**, *4*, 45.
[98] S. Walheim, M. Böltau, J. Mlynek, G. Krausch, U. Steiner, *Macromolecules* **1997**, *30*, 4995.
[99] C. Ton-That, A. Shard, R. Bradley, *Polymer* **2002**, *43*, 4973.
[100] H. Hauser, K. Mühlbach, O. Höhn, R. Müller, S. Seitz, J. Rühe, S. W. Glunz, B. Bläsi, *Opt. Express* **2020**, *28*, 10909.
[101] R. H. Siddique, Y. J. Donie, G. Gomard, S. Yalamanchili, T. Merdzhanova, U. Lemmer, H. Hölscher, *Sci. Adv.* **2017**, *3*, e1700232.
[102] Y. J. Donie, M. Smeets, A. Egel, F. Lentz, J. B. Preinfalk, A. Mertens, V. Smirnov, U. Lemmer, K. Bittkau, G. Gomard, *Nanoscale* **2018**, *10*, 6651.
[103] F. Pratesi, M. Burresi, F. Riboli, K. Vynck, D. S. Wiersma, *Opt. Express* **2013**, *21*, A460.
[104] S. Nanz, A. Abass, P. M. Piechulla, A. Sprafke, R. B. Wehrspohn, C. Rockstuhl, *Opt. Express* **2018**, *26*, A111.
[105] S. Schauer, M. Worgull, H. Hölscher, *Soft Matter* **2017**, *13*, 4328.
[106] F. Mayer, D. Ryklin, I. Wacker, R. Curticean, M. Čalkovský, A. Niemeyer, Z. Dong, P. A. Levkin, D. Gerthsen, R. R. Schröder, M. Wegener, *Adv. Mater.* **2020**, *32*, 2002044.
[107] S. Schauer, R. Schmager, R. Hünig, K. Ding, U. W. Paetzold, U. Lemmer, M. Worgull, H. Hölscher, G. Gomard, *Opt. Mater. Express* **2018**, *8*, 184.
[108] Q.-Q. Liu, Y.-Y. Zhao, M.-L. Zheng, X.-M. Duan, *Appl. Phys. Lett.* **2017**, *111*, 223102.
[109] M. Rothammer, M.-C. Heep, G. von Freymann, C. Zollfrank, *Cellulose* **2018**, *25*, 6031.
[110] A. Berg, R. Wyrwa, J. Weisser, T. Weiss, R. Schade, G. Hildebrand, K. Liefeith, B. Schneider, R. Ellinger, M. Schnabelrauch, *Adv. Eng. Mater.* **2011**, *13*, B274.
[111] O. Kufelt, A. El-Tamer, C. Sehring, S. Schlie-Wolter, B. N. Chichkov, *Biomacromolecules* **2014**, *15*, 650.
[112] G. Della Giustina, A. Gandin, L. Brigo, T. Panciera, S. Giulitti, P. Sgarbossa, D. D'Alessandro, L. Trombi, S. Danti, G. Brusatin, *Mater. Des.* **2019**, *165*, 107566.
[113] V. Hwang, A. B. Stephenson, S. Magkiriadou, J.-G. Park, V. N. Manoharan, *Phys. Rev. E* **2020**, *101*, 012614.
[114] B. D. Wilts, X. Sheng, M. Holler, A. Diaz, M. Guizar-Sicairos, J. Raabe, R. Hoppe, S.-H. Liu, R. Langford, O. D. Onelli, D. Chen, S. Torquato, U. Steiner, C. G. Schroer, S. Vignolini, A. Sepe, *Adv. Mater.* **2018**, *30*, 1702057.
[115] L. Cortese, L. Pattelli, F. Utel, S. Vignolini, M. Burresi, D. Wiersma, *Adv. Opt. Mater.* **2015**, *3*, 1337.
[116] M. Florescu, S. Torquato, P. Steinhardt, *Proc. Natl. Acad. Sci. USA* **2009**, *106*, 20658.
[117] M. Florescu, S. Torquato, P. Steinhardt, *Appl. Phys. Lett.* **2010**, *97*, 201103.
[118] A. Arsenault, F. Fleischhaker, G. von Freymann, V. Kitaev, H. Miguez, A. Mihi, N. Tétreault, E. Vekris, I. Manners, S. Aitchison, D. Perovic, G. Ozin, *Adv. Mater.* **2006**, *18*, 2779.
[119] M. Florescu, P. Steinhardt, S. Torquato, *Phys. Rev. B - Condens. Matter Mater. Phys.* **2013**, *87*, 165116.
[120] W. Man, M. Florescu, E. Williamson, Y. He, S. Hashemizad, B. Leung, D. Liner, S. Torquato, P. Chaikin, P. Steinhardt, *Proc. Natl. Acad. Sci. USA* **2013**, *110*, 15886.
[121] N. Muller, J. Haberko, C. Marichy, F. Scheffold, *Optica* **2017**, *4*, 361.
[122] S. F. Liew, J.-K. Yang, H. Noh, C. F. Schreck, E. R. Dufresne, C. S. O'Hern, H. Cao, *Phys. Rev. A* **2011**, *84*, 063818.
[123] W. Man, M. Florescu, K. Matsuyama, P. Yadak, G. Nahal, S. Hashemizad, E. Williamson, P. Steinhardt, S. Torquato, P. Chaikin, *Opt. Express* **2013**, *21*, 19972.
[124] S. Sellers, W. Man, S. Sahba, M. Florescu, *Nat. Commun.* **2017**, *8*, 14439.
[125] J. Haberko, F. Scheffold, *Opt. Express* **2013**, *21*, 1057.
[126] N. Tétreault, G. von Freymann, M. Deubel, M. Hermatschweiler, F. Pérez-Willard, S. John, M. Wegener, G. A. Ozin, *Adv. Mater.* **2006**, *18*, 457.
[127] A. Ledermann, D. Wiersma, M. Wegener, G. von Freymann, *Opt. Express* **2009**, *17*, 1844.
[128] N. Muller, J. Haberko, C. Marichy, F. Scheffold, *Adv. Opt. Mater.* **2014**, *2*, 115.
[129] J. B. Pendry, A. Aubry, D. R. Smith, S. A. Maier, *Science* **2012**, *337*, 549.
[130] Y. Liu, X. Zhang, *Nanoscale* **2012**, *4*, 5277.
[131] R. Schittny, A. Niemeyer, F. Mayer, A. Naber, M. Kadic, M. Wegener, *Laser Photon. Rev.* **2016**, *10*, 382.
[132] A. Niemeyer, F. Mayer, A. Naber, M. Koirala, A. Yamilov, M. Wegener, *Opt. Lett.* **2017**, *42*, 1998.
[133] F. Martelli, S. D. Bianco, A. Ismaelli, G. Zaccanti, *Propagation Through Biological Tissue and Other Diffusive Media: Theory, Solutions, and Software*, 1st ed., SPIE Press, Bellingham, WA **2010**.
[134] R. Schittny, A. Niemeyer, M. Kadic, T. Bückmann, A. Naber, M. Wegener, *Opt. Lett.* **2015**, *40*, 4202.
[135] E. H. Kerner, *Proc. Phys. Soc. B* **1956**, *69*, 802.
[136] S. Longhi, *Laser Photonics Rev.* **2009**, *3*, 243.
[137] M. Cohen, C. Jörg, Y. Lumer, Y. Plotnik, E. Waller, J. Schulz, M. von Freymann, G. Segev, *Light Sci. Appl.* **2020**, *9*, 200.
[138] M. Heinrich, M. Rechtsman, F. Dreisow, S. Nolte, M. Segev, A. Szameit, *Opt. Lett.* **2014**, *39*, 3599.
[139] M. Rechtsman, J. Zeuner, Y. Plotnik, Y. Lumer, D. Podolsky, F. Dreisow, S. Nolte, M. Segev, A. Szameit, *Nature* **2013**, *496*, 196.
[140] J. Zeuner, M. Rechtsman, S. Nolte, A. Szameit, *Opt. Lett.* **2014**, *39*, 602.
[141] H. Kondakci, A. Szameit, A. Abouraddy, D. Christodoulides, B. Saleh, *Optica* **2016**, *3*, 477.
[142] K. Tschernig, A. Jiminez-Galan, D. N. Christodoulides, M. Ivanov, K. Busch, M. A. Bandres, A. Perez-Leija, *Nat. Commun.* **2021**, *12*, 1974.

Maximilian Rothammer is carrying out his Ph.D. under the supervision of Prof. Dr. Cordt Zollfrank at the Chair for Biogenic Polymers at the Technical University of Munich (TUM). He completed the studies of materials science and engineering with an M.Sc. degree at the Friedrich-Alexander University Erlangen-Nuremberg. His scientific interests are the development and synthesis of novel bio-based photopolymers as resists for additive manufacturing of submicron bioinspired architectures and as UV-crosslinkable inks and coatings.

Cordt Zollfrank received his Ph.D. in forest science at TUM, Germany, in 2000. He worked as a postdoctoral researcher and as group leader at the University of Erlangen-Nuremberg. Since 2011, he is professor for biogenic polymers at TUM Campus Straubing. His research focuses on applying bioinspired synthetic methods to the development of innovative structural and functional materials. A key area of his work is the formation of biogenic structures and their conversion to composite materials for engineering and biomedical applications. The fundamental chemical and physical transformation processes involved in these conversions are investigated at each level of the structural hierarchy.

Kurt Busch received his Ph.D. degree in physics from Universität Karlsruhe (TH), Germany, in 1996. He was a postdoctoral researcher at the University of Toronto and head of a Junior Research Group within the DFG Emmy-Noether Programme at Universität Karlsruhe (TH). Professor positions at University of Central Florida and Universität Karlsruhe (TH) followed. Since 2011, he is full professor at the Humboldt-Universität zu Berlin and group leader at the Max Born Institut. He is fellow of the OSA. His research interests encompass quantum photonics and nanophotonics, computational photonics, theory of light propagation, light-matter interaction in strongly scattering systems, and fluctuation-induced phenomena.

Georg von Freymann received his Ph.D. degree in physics from Universität Karlsruhe (TH), Germany, in 2001. After spending his postdoctoral years at Forschungszentrum Karlsruhe and at University of Toronto, he headed a Junior Research Group in the DFG Emmy-Noether programme at the Karlsruhe Institute of Technology (KIT). Since 2010, he is full professor for experimental physics at the Technische Universität Kaiserslautern, Germany. Since 2013, he is head of the department for materials characterization and testing at the Fraunhofer Institute for Industrial Mathematics. His research interests include 3D nanofabrication technologies, photonic crystals, quasicrystals, and metamaterials, terahertz technology, and spin-wave optics.